



NASA Public Access

Author manuscript

Bull Am Meteorol Soc. Author manuscript; available in PMC 2020 February 15.

Published in final edited form as:

Bull Am Meteorol Soc. 2019 February 15; 100(1): 93–121. doi:10.1175/BAMS-D-17-0180.1.

Cloud System Evolution in the Trades—CSET:

Following the Evolution of Boundary Layer Cloud Systems with the NSF/NCAR GV

Bruce Albrecht,

Dept. Atmospheric Science; Univ. Miami

Virendra Ghat,

Argonne National Laboratory

Johannes Mohrmann,

Dept. Atmos. Sciences, Univ. Washington

Robert Wood,

Dept. Atmos. Sciences, Univ. Washington

Paquita Zuidema,

Dept. Atmospheric Science; Univ. Miami

Christopher Bretherton,

Dept. Atmos. Sciences, Univ. Washington

Christian Schwartz,

Argonne National Laboratory

Edwin Eloranta,

Univ. Wisconsin

Susanne Glienke,

Atmos. Sci. Program, Michigan Technological Univ.

Shaunna Donaher,

Emory University

Mampi Sarkar,

Dept. Atmospheric Science; Univ. Miami

Jeremy McGibbon,

Dept. Atmos. Sciences, Univ. Washington

Alison Nugent,

Dept. Atmospheric Science, Univ. Hawaii

Raymond A. Shaw,

Atmos. Sci. Program, Michigan Technological Univ.

Jacob Fugal,

Max Plank Institute of Chemistry

Corresponding Author: Bruce Albrecht, balbrecht@miami.edu.

Patrick Minnis,
Science Systems and Applications, Inc., NASA Langley Research Center

Robindra Paliknoda,
Science Systems and Applications, Inc., NASA Langley Research Center

Louis Lussier,
Earth Observing Laboratory, NCAR

Jorgen Jensen,
Earth Observing Laboratory, NCAR

J. Vivekanandan,
Earth Observing Laboratory, NCAR

Scott Ellis,
Earth Observing Laboratory, NCAR

Peisang Tsai,
Earth Observing Laboratory, NCAR

Robert Rilling,
Earth Observing Laboratory, NCAR, Boulder, Colorado

Julie Haggerty,
Earth Observing Laboratory, NCAR

Teresa Campos,
Atmospheric Chemistry Observations and Modeling Laboratory, NCAR

Meghan Stell,
Earth Observing Laboratory, NCAR, Boulder, Colorado

Michael Reeves,
Earth Observing Laboratory, NCAR

Stuart Beaton,
Earth Observing Laboratory, NCAR

John Allison,
Earth Observing Laboratory, NCAR

Gregory Stossmeister,
Earth Observing Laboratory, NCAR

Samuel Hall,
Earth Observing Laboratory, NCAR

Sebastian Schmidt
Univ. of Colorado

Abstract

The Cloud System Evolution in the Trades (CSET) study was designed to describe and explain the evolution of the boundary layer aerosol, cloud, and thermodynamic structures along trajectories

within the north-Pacific trade-winds. The study centered on 7 round-trips of the NSF NCAR Gulfstream V (GV) between Sacramento, CA and Kona, Hawaii between 1 July and 15 August 2015. The CSET observing strategy was to sample aerosol, cloud, and boundary layer properties upwind from the transition zone over the North Pacific and to resample these areas two days later. GFS forecast trajectories were used to plan the outbound flight to Hawaii with updated forecast trajectories setting the return flight plan two days later. Two key elements of the CSET observing system were the newly developed HIAPER Cloud Radar (HCR) and the High Spectral Resolution Lidar (HSRL). Together they provided unprecedented characterizations of aerosol, cloud and precipitation structures that were combined with *in situ* measurements of aerosol, cloud, precipitation, and turbulence properties. The cloud systems sampled included solid stratocumulus infused with smoke from Canadian wildfires, mesoscale cloud-precipitation complexes, and patches of shallow cumuli in very clean environments. Ultra-clean layers observed frequently near the top of the boundary layer were often associated with shallow, optically thin, layered veil clouds. The extensive aerosol, cloud, drizzle and boundary layer sampling made over open areas of the Northeast Pacific along 2-day trajectories during CSET is unprecedented and will enable modeling studies of boundary layer cloud system evolution and the role of different processes in that evolution.

1) Introduction and Motivation

Boundary-layer clouds in the form of stratocumulus and small marine cumulus are the most frequently observed cloud types over the Earth's oceans, are the most abundant types globally (Norris, 1998) and have an important impact on the Earth's radiation budget (Hartmann and Short 1980). The energy and moisture fluxes associated with these clouds are critical in maintaining the thermodynamic structure of the lower troposphere. Thus, both the turbulent mixing and the radiative impact on the surface associated with marine boundary layer (MBL) clouds need to be adequately parameterized in large-scale models (Bony and Dufrense, 2005). The inadequate representation of MBL cloud processes in large-scale models continues to be a major contributor to model uncertainties in cloud feedback representations-- particularly in subtropical anticyclone regions (Zhang et al. 2005, Wyant et al. 2010, Teixeira et al. 2011, Soden and Vecchi, 2011).

The stratocumulus (Sc) regimes associated with the eastern flank of the subtropical anticyclones evolve into fair-weather cumulus (Cu) regimes in the persistent trade winds associated with the anticyclones. The high albedo and large areal extent of Sc corresponds to a significant reduction in surface solar heating (e.g., Hartmann et al, 1992; Klein and Hartmann 1993). Cu, on the other hand, play a fundamental role in the regulation of ocean surface evaporation and convergence of moisture into deep convective regions (e.g., Tiedtke 1989, Neggers et al. 2007), and therefore the global hydrological cycle. The transition from shallow, cloud-topped MBLs in the cool subtropics to broken trade cumulus over the warm tropics (Bretherton and Wyant 1997, Bretherton et al. 1999, Sandu and Stevens 2011) occurs over all subtropical ocean basins and sets the climatological distribution of cloud cover (Albrecht et al. 1995). In the Sc-Cu transition, the MBL evolves from a well-mixed, single layer topped with extensive clouds under a sharp inversion, into a deeper, vertically-stratified

structure containing cumulus clouds with greatly reduced cover capped by a weaker and more diffuse inversion.

Cloud top entrainment is one of the key processes driving the stratocumulus-to-cumulus transition. The MBL deepening associated with entrainment causes decoupling: the separation of the MBL into two distinct layers with limited exchange between them. Decoupling that starves the Sc of their surface moisture source and increased entrainment of dry air into the MBL due to more energetic cumulus plumes lead to their breakup. They are replaced by broken Cu whose tops are more variable, with a greater spread of cloud top height and fewer reaching the inversion. Cloud top entrainment profoundly impacts the type and coverage of clouds within the MBL because it plays such an important role in the MBL moisture, heat and momentum budgets (Lilly 1968, Bretherton and Wyant 1997, Wyant et al. 1997, Stevens 2002, Stevens et al. 2002). In addition, cloud top entrainment controls how MBL clouds respond to increased greenhouse gases (Caldwell and Bretherton 2009) and atmospheric aerosols (Ackerman et al. 2004, Wood 2007, Bretherton et al. 2007).

Cloud System Evolution in the Trades (CSET) was developed to describe and explain the evolution of the MBL aerosol, cloud, and thermodynamic structures along trajectories within the north-Pacific trade-winds using the NSF/NCAR Gulfstream V (GV, formerly known as HIAPER (High Performance Instrumented Airborne Platform for Environmental Research)) on flights between California and Hawaii. The long range of the NSF GV allowed for the sampling of air masses on low-level trajectories extending from California to Hawaii and then a re-sampling of these same air masses on the return flight two days later.

The stratocumulus-trade cumulus transition is often sharply defined as shown in Fig. 1. The upstream part of the transition was arguably first examined with five NCAR Electra flights undertaken in 1975 and documented in Brost et al. (1982a; 1982b) and Albrecht et al. (1985). The Atlantic Stratocumulus Transition Experiment (ASTEX; Albrecht et al., 1995a) brought new cloud remote sensors to the field, as well as an explicit Lagrangian sampling approach. Two Lagrangian experiments each tracked air masses for 36-48 hours using instrumented aircraft (Bretherton and Pincus, 1995; Bretherton et al., 1995). The ASTEX Lagrangian studies, however, were not made in classic trade-wind flow and lacked aircraft-based lidar and radar observations needed to provide a detailed mapping of cloud and precipitation structures.

More recent regional observational and modeling studies have also focused on the MBL cloud, aerosol, and precipitation structures within the MBL in the cloud regimes associated with the transition. During the VAMOS Ocean-Cloud-Atmosphere-Land Study Regional Experiment (VOCALS-REx, 2008) a comprehensive study was made of the aerosol-cloud-and precipitation properties of stratocumulus clouds in the southeastern Pacific (Wood et al., 2011a; Mechoso et al., 2014). The observational and modeling studies focused on the stratocumulus structures extending westward from the west coast of Chile. The VOCALS studies have brought important new insight into the extreme aerosol-cloud interactions associated with Pockets of Open Cells (POCs) and the role of mesoscale organizations in those interactions (Wood et al. 2011b; Berner et al., 2011; Kazil et al., 2012; Wang et al., 2010; Berner et al., 2013) In addition, VOCALS provided a comprehensive description of

the aerosol, cloud, precipitation and MBL structures as the MBL deepens along 20 °S for ~1500 km westwards from the Chilean coast (Bretherton et al., 2010a). The VOCALS results provide an important baseline for comparing the microphysical and macrophysical structure of the stratocumulus clouds sampled during CSET.

VOCALS did not extend into the trade-wind cumulus regime downwind of the main Sc deck. Much of the early observational work on small cumuli in the trade wind boundary layer was conducted using *in situ* aircraft observations. But there are inherent limitations to this approach since the volume sampled during an aircraft penetration is relatively small and it is difficult to study the time evolution of the vertical structure. Furthermore, it is difficult to determine exactly where in the cloud the measurements are being made and at what stage of the life cycle the cloud is being sampled. During the Rain in Cumulus over the Ocean (RICO; Rauber et al., 2007) field campaign some important issues were addressed concerning aerosol cloud interactions (e.g. Gerber et al. 2008); but the RICO aircraft measurements did not benefit from good cloud radar observations. During the Barbados Aerosol Cloud Experiment (BACEX, 2010) *in-situ* cloud observations in fair weather cumulus clouds were made with the CIRPAS Twin Otter research aircraft (Jung et al., 2012) and with an upward-pointing Frequency Modulated Continuous Wave (FMCW) cloud radar. The RICO and BACEX observations provided insight into entrainment and precipitation processes in small cumulus clouds (e.g., Nuijens et al., 2009; Minor et al., 2012; Zuidema et al., 2012a) and provide a background for the CSET observations in the fair weather cumulus regions sampled.

Although recent field programs have advanced our understanding of processes operating in the two cloud regimes central to CSET, they have not directly addressed the stratocumulus to trade cumulus transition. A recent study, DOE MAGIC (the Marine ARM GPCI Investigation of Clouds), involved ship-borne measurements from a container ship that made regular transects between Los Angeles and Hawaii from October 2012 to September 2013 using the ARM Mobile Facility (Zhou et al., 2015). In addition to *in situ* observations, the clouds above the ship were sampled using lidar and radar observations in both the stratocumulus and the trade cumulus regime. Although the cloud transition is well defined in some of the transects, the slow movement of the ship limits the usefulness of these observations for Lagrangian studies. The long range of the GV uniquely positions it to provide in-situ measurements of aerosols and cloud microphysics, including interactions with the free troposphere across the entire transition and to track the evolutions of cloud systems.

The subtropical NE Pacific stratocumulus to cumulus transition sampled during CSET flights has long been a canonical modeling challenge. Two benchmark cases of Sc-Cu transition have been used for international modeling inter-comparison efforts as part of the Global Atmospheric System Study (GASS) and its predecessor, GCSS. The first of these was from the 1992 NE Atlantic ASTEX project described previously (Bretherton et al. 1995, 1999; van der Dussen et al. 2013). The second was a satellite derived composite (Sandu et al. 2010) of several thousand Lagrangian trajectories based on MODIS cloud observations with trajectories based on ECMWF reanalyses. Neither case includes a good accompanying set of aerosol observations in or above the boundary layer or the robust statistics on

horizontal cloud and precipitation inhomogeneity that a cloud radar and lidar combination can provide (e. g. Bretherton et al. 2010b; Wood et al. 2011b).

LES models have become a robust tool for Lagrangian simulations of subtropical cloudiness transitions, but there are few good datasets for comprehensively testing these simulations. In particular, we lack adequate observations of the coupled evolution of aerosol, cloud droplet number concentration and precipitation during such transitions. The MAGIC AMF deployment provided a ship-based perspective on this problem (McGibbon and Bretherton, 2017; Zhou et al., 2015), but the long range of the GV allows *in situ* measurements of aerosols and cloud microphysics, including interactions with the free troposphere, across the entire transition. By resampling the same boundary-layer air masses on the return flights as the outbound flights, the measurements can naturally be compared with the Lagrangian LES and SCM simulations that have proved to be valuable for constructing and analyzing better models of MBL cloud and its sensitivity to environmental conditions.

Based on this background, the following scientific goals were set for CSET:

- Define the evolution of the cloud, precipitation and aerosol fields in stratocumulus clouds as they transition into the fair-weather cumulus regimes within the subtropical easterlies over the northern Pacific.
- Examine the cloud microphysical properties and processes as a function of boundary-layer depth, towards assessing the relative contributions of internal and external processes to boundary-layer cloud-system evolution.
- Evaluate the relative importance of boundary layer deepening and precipitation processes in driving boundary layer decoupling and cloud breakup.
- Provide comprehensive case studies and integrated data sets to evaluate and improve process models, LES, and GCMs to describe and explain cloud system evolution in the trades.

CSET was designed to describe and explain the evolution of the MBL aerosol, cloud, and thermodynamic structures along trajectories within the north-Pacific trade-winds. The NSF/NCAR GV supported by the NCAR Earth Observing Laboratory (EOL) served as the principal source of the observations used in this study. The observational effort included characterization of the cloud, precipitation and aerosol fields in the stratocumulus and the fair-weather cumulus regimes within the subtropical easterlies over the northern Pacific. These characterizations along trajectories were designed to aid in our understanding and simulation of the transition between the two convective regimes. The Lagrangian approach allowed us to track air masses as they flowed from colder to warmer sea surface temperatures and thus minimize uncertainties in the large-scale forcing due to horizontal advection in the lower troposphere. This approach facilitates comparison with Lagrangian model simulations and the isolation of critical physical processes operating in the cloud evolution.

2. Experiment Design

The NSF/NCAR GV was selected for CSET because of its range and endurance in addition to its observational capabilities. Two modes of operations were implemented for the GV flights between the west coast of California and Hawaii. The first—a surveying mode—included radar and lidar remote sensing of the clouds and MBL from an altitude of about 6 km (20 kft) altitude along transects. In this mode, dropsondes were deployed to obtain the thermodynamic and wind structure in and above the MBL upstream and downstream from the StCu to Cu transition zone. The second—*in situ* mode—involved detailed profiling in the subcloud, cloud layer, and across the top of the boundary layer in three to four selected areas upstream and downstream of the transition zone. The lidar and cloud radar remained critical components of the low-level sampling. These two sampling modes were necessary, since the GV would not have the range to do all the sampling at low levels. With about half of the flight flown at a higher altitude, the GV flights from California to Hawaii were possible.

a. Instrumentation

A full suite of probes on the GV were used for *in situ* measurements of aerosol, cloud, precipitation, and turbulence properties. The instrumentation is listed in Table 1 and described in detail on the EOL website (<http://www.eol.ucar.edu/raf/instruments/doc/>). The GV was well-instrumented for making *in situ* characterizations of the mean and turbulent wind and thermodynamic structures below, in and above the cloud layer. Further, aerosol, cloud and precipitation observations were made from the G-V using several probes. The GV aerosol measurements were made using a Ultra-High Sensitivity Aerosol Spectrometer (UHSAS) that samples particles in the nominal range of 0.06-1.0 microns (but reduced to 0.075-1.0 microns for CSET). A Condensation Nuclei (CN) counter gives the total aerosol concentrations greater than a threshold of about 10 nanometers. The cloud particle distributions were measured with a cloud droplet probe (CDP) and the precipitation sized water droplets were obtained using an optical array probe (OAP 2-D Precipitation Probe and a 3-D CPI). The second generation Holographic Detector for Clouds (HOLODEC; Fugal and Shaw, 2009; Spuler and Fugal, 2011) was a new instrument used on the GV to size cloud and drizzle droplets (in the range of about 6 μm to 1 mm) and to determine the three-dimensional position of hydrometeors using digital in-line holography. The unique aspects of HOLODEC are that the sample volume measured per second (about 43 cm^3) is not speed dependent and the effects produced by shattering from the aperture edges can be identified and eliminated. Most significantly, it is possible to measure cloud droplet size distributions from individual localized sample volumes with the largest dimension being 130 mm, instead of an average over more than 10 m (e.g. for a measurement from CDP at 10 Hz), as well as determine the positions of the droplets within that volume. Post-flight analyses of the holograms recorded at 3.3 Hz produce size distributions for all samples in cloud and precipitation areas sampled during CSET by HOLODEC (Glienke et al, 2017).

Ozone and carbon monoxide measurements were made using the Fast Response Ozone (F03_AD) and the Carbon Monoxide (Aero-Laser VUV) instruments supported by the Community Airborne Research Instrumentation (CARI) group in Atmospheric Chemistry Observations and Modeling (ACOM). Upward and downward longwave and short wave

radiative fluxes were measured from broadband sensors (Kipp & Zonen broadband radiometers) and the HIAPER Airborne Radiation Package (HARP) provided downward spectral irradiances.

Two key remote sensing systems used on the GV during CSET were the HIAPER Cloud Radar (HCR) developed by NCAR EOL and the High Spectral Resolution Lidar (HSRL) developed under the NSF HIAPER Aircraft Instrumentation Solicitation (HIAS; ref). These remote sensing instruments were used to define macroscopic and microscopic cloud properties as the GV flew above, below, and in the clouds. The HCR characteristics are described in Rauber et al. (2017) and in Schwartz et al. (2018). It is a pulsed Doppler radar that operates at a 95 GHz frequency (3 mm wavelength) and has a sensitivity of -39.6 dBZ at 1 km range. The HCR in CSET was operated with a temporal resolution of 0.5 sec, which for air speeds of the GV gives a horizontal resolution of 50-100 m. The vertical range resolution of 20 m makes the HCR ideal for observing stratocumulus and cumulus clouds and their associated precipitation structures. The first three Doppler spectra moments (reflectivity, mean Doppler velocity and spectral width) calculated using the pulse-pair technique were displayed in real-time on the aircraft and recorded and archived for processing. In addition, the raw data that give phase and amplitude from the inphase (I) and quadrature-phase (Q) signals for each pulse were recorded and archived for each flight. These raw I and Q data were used in post processing to calculate the full radar Doppler spectrum and its first four moments (Schwartz et al. 2018).

A special wing pod was developed for mounting the HCR on the GV (Fig. 2). The pod design allowed a steerable reflector to extend ahead of the wing to allow for sampling both below and above the aircraft. The reflector was also actively controlled to remove pointing errors due to pitch variations on the GV (Vivekanandan et al. 2014). Operating at 95 GHz frequency, the HCR suffers from signal attenuation due to absorption by water vapor and oxygen. Corrections were made using dropsonde data obtained on CSET and applying a method described by Ulaby (1981) when the radar is looking downward from above the clouds.

The HCR characterized the cloud and precipitation structures and provided a measure of cloud-top heights during both pointing directions. Its volume sampling is particularly suited for characterizing light precipitation--a highly-localized and variable quantity (see, e.g., Wood, 2005). Aircraft-based 95-GHz radar measurements have a proven track record for advancing our understanding of the role of precipitation in MBL clouds (Vali et al., 1998; Stevens et al., 2003; Wood et al., 2011a). Ground-based and airborne cloud radars have been used to characterize the vertical velocity structure of stratocumulus clouds (e.g. Lothon et al. 2004; Ghate et al. 2010) and of shallow cumulus clouds (e.g. Geerts and Miao, 2005; Ghate et al., 2011; Wang and Geerts, 2012). During non-precipitating conditions (reflectivity < -15 dBZ) when the cloud droplets have negligible fall velocity, the measured Doppler velocity corrected for the aircraft motion can be used as a proxy for the vertical air motion (Lothon et al. 2004). During precipitating conditions, either (a) the fall velocity of precipitating drops can be removed from the measured Doppler velocity corrected for the aircraft motion to retrieve the vertical air motion or (b) the method proposed by Luke and Kollias (2013) that uses the higher order moments of radar Doppler spectrum to distinguish between the echoes

due to cloud droplets and drizzle drops and can be used to calculate the vertical air motion. Also, when drops larger than 1.6 mm in diameter exist in the radar sample volume, a “notch” in the Doppler spectrum can be observed (Kollias et al. 2000) due to scattering by the drops in the Mie regime. The presence of the Mie notch allows the retrieval of air vertical velocity (e.g. Kollias et al, 2000; Giangrande et al 2012; Ming et al, 2017). Mie notches were observed frequently during CSET and will be used to deduce vertical air motions in more heavily precipitating clouds using the HCR.

The HSRL used in CSET is an eye-safe calibrated lidar system that measures backscatter cross section, extinction and depolarization properties of atmospheric aerosols and clouds (Razenkov et al. 2002 and 2008). The HSRL provides estimates of cloud base heights while pointing up and cloud top heights while pointing down, together with aerosol properties, derived from profiles of backscatter cross-section, extinction cross-section and depolarization ratio at 532 nm at a temporal resolution of ~0.5 sec. The range resolution of the retrieved backscatter cross-section profiles is ~30 m while that of extinction profile is ~300 m (Morley et al., 2012). The circular depolarization ratio observed by the HSRL can distinguish between different aerosol types (Burton et al. 2011). On the GV the laser transmitter and telescope can be manually oriented to face either upward or downward (see Fig. 2) through windows on the top and bottom of the fuselage.

The first three Doppler spectral moments from the HCR, and the backscatter and extinction cross-section from the HSRL were combined to retrieve drizzle drop size distributions while pointing up using the technique proposed by O’Connor et al. (2005). For optically thin clouds that were detected by both the HCR and the HSRL, the cloud drop size distributions were also retrieved (see Wood et al, 2018 for an example from a CSET flight).

When the aircraft was flying above the MBL in surveying mode (at a flight level of ~6 km), the HCR and HSRL were operated pointing downwards to observe MBL cloud and aerosol fields from the flight level to the surface. For clouds that are 5 km below the aircraft, the HCR minimum detectable reflectivity is about -23 dBz. On flight legs below the cloud base (near surface), the HCR and HSRL were facing upwards to sample clouds and aerosols above the flight level. During the flight legs in the clouds, the HCR and HSRL were pointing downwards to characterize the sub-cloud layer aerosol and precipitating fields. The combined HCR and HSRL retrievals were used to estimate cloud boundaries for the flights flown (Schwartz et al., 2018).

To further complement the HCR and HSRL measurements, a 4-channel zenith-pointing 183 GHz radiometer was flown to provide liquid water path (LWP) and water vapor estimates. This radiometer is similar to one used during the VOCALS project (Zuidema et al., 2012b). Such radiometers have the potential to provide an additional fundamental cloud observation that can help connect the observations to models and quantify the cloud albedo and rain susceptibilities, or how much the cloud albedo and rain vary as a function of droplet number and LWP (Terai et al., 2012; Painemal and Zuidema, 2013). Further, they can provide a geophysical constraint on lidar and radar-specific retrievals, such as a combination with the attenuation-corrected HCR reflectivity data to develop a simple Z-LWC relationship for

nonprecipitating clouds ($\text{dBz} < -15$). The 183 GHz channels are also fully attenuated in moist environments, limiting their application to the drier northern stratocumulus clouds.

Dropsondes were launched from the GV during CSET using an AVAPSTM (Airborne Vertical Atmospheric Profiling System (https://www.eol.ucar.edu/observing_facilities/avaps-dropsonde-system)). *In-situ* data collected from the sondes' sensors were transmitted back in real time to an onboard aircraft data system via radio link. Input for times and locations of the drop releases were sent from the flight scientist on the GV to the CSET home base in Sacramento where an operator these would send instructions to the GV to trigger the sonde launches at the designated points.

b. Supporting tools and observations

A key element of CSET was the EOL Field Catalog II (<http://catalog.eol.ucar.edu/cset>). The Field Catalog was used extensively for mission planning, real-time access to aircraft observations and satellite products during the missions, and for posting reports of mission planning, operations, and summaries. The catalog was used for documentation of the mission operations and serves as an archive reference for data collected during CSET. After the mission the catalog is being used extensively in playback mode of all the aircraft observations and ancillary products collected during each mission. The Field Catalog is developed and maintained by EOL's Data Management and Services Facility (DMS) and catalogs for past field projects are available at: <http://catalog.eol.ucar.edu/>. (The field catalog is identified as <https://doi.org/10.5065/D6SQ8XFB>. EOL Field Catalog; UCAR/NCAR - Earth Observing Laboratory, 1995-present).

Imagery from the 15th Geostationary Operational Environmental Satellite (GOES 15) satellite observations (centered over 135 °W longitude) was used to define the larger-scale (greater than 100 km x 100 km) cloud fields using near-real-time visible and infrared images (Ch1-Ch4; and high resolution; 1km x 1km visible at nadir). Cloud property fields derived from the GOES observations were provided by the NASA Langley Satellite Cloud and Radiation Property retrieval System (SatCORPS; <https://satcorps.larc.nasa.gov>) estimated using the methods outlined by Minnis et al. (2008) and Sun-Mack et al. (2014) and included broadband albedo, cloud-top height, cloud droplet concentrations, cloud droplet effective radius, liquid water path, and other cloud properties (see the Field Catalog Maps app for a full list). The satellite products were available in near real time from the Field Catalog and were instrumental for flight planning and for in-flight updates during the missions. All satellite product images produced during CSET are available in the playback mode with the Field Catalog Maps application.

3. Observing Strategy and Mission Operations

The general sampling strategy employed in CSET was to use the GV to sample clouds and MBL structures within trajectories extending westward along the southern periphery of the North East Pacific. This Lagrangian approach is designed to minimize uncertainties in the large-scale forcing due to horizontal advection in the lower troposphere as air masses move from cold to warm SSTs. Thus, the observing strategy was to sample aerosol, cloud, and MBL properties in areas upwind from the transition zone over the North East on GV flights

originating from Sacramento and ending in Kona Hawaii. The GV and crew would then spend one day in Kona with a return flight to Sacramento two days after the outbound flight. The return (inbound) flight was planned so that GV could do low-level sampling in the same air masses that were sampled two days earlier during the outbound flights.

Since the GV range is substantially reduced when flown at lower levels, the amount of time that could be flown for low-level boundary sampling was limited to about 50% of the flight time between California and Hawaii. Thus a strategy was developed that allowed for two types of sampling—1) surveying and 2) *in situ*. In the surveying mode, the MBL structures, cloud properties, and aerosol distributions were sampled using the HCR and HSRL operating in a downward facing mode to sample from the flight level to the surface. This leg was typically flown at about 6 km (20 kft). Generally, *in situ* cloud and MBL observations were made in three targeted areas along these transects on profiling flight legs flown in and just above the BL over a distance of 1500 to 1800 km). For the return flights from Hawaii, trajectory analyses were used to identify air masses sampled two days earlier on the flight outbound from California. The flights between Sacramento California and Kona Hawaii were over a distance of about 4000 km.

Flight plans for the outbound flights originating from Sacramento were based on 500 m trajectory forecasts that were made using HYSPLIT (Hybrid Single Particle Lagrangian Integrated Trajectory Model) with NCEP GFS forecasts and GDAS analyses. The trajectory forecasts used for the outbound planning comprised a swarm of 28 forward planetary boundary layer constant height trajectories made using the 12 UTC 0.25° forecast from the day before flight. The initial points for the 28 trajectories were chosen using the current GOES satellite visible imagery to identify areas of cloud transition and were prepared for the mission planning meetings that were held afternoon before an outgoing flight from Sacramento the next day. An example of a trajectory swarm forecast is shown in Fig. 6 with trajectories overlain on the GOES visible satellite imagery with the trajectory starting points for a flight planned for July 27. These trajectories show the starting points (stars) and the 48-hour end points (squares) for the 28 trajectories. During the mission planning meetings, the science team examined the trajectory swarms and estimated which of the endpoints of these trajectories would be in the range of the GV on the return flight two days later. On the basis of this process, the initial points to be sampled were selected and the endpoints were set as tentative sampling areas for the return flight. These flight plans were then shared with the GV pilots who would assess the feasibility of the proposed flights and would suggest any modifications needed to make the planned flights achievable.

Once in Kona, there would be another mission planning meeting the afternoon between flight days. During this meeting, updated trajectory end points were used to set the flight track back to Sacramento, using 12 UTC day-before-return-flight analysis and forecasts and the outbound flight path. For the RF10 July 27 example shown in Fig 3, the beginning and end points of the 9 trajectories selected for the sampling sequence are shown in Fig. 3b. These trajectories are overlaid on the satellite image from 28 July to show (after the fact) how the selected trajectories lined up with the clouds observed one day after the outgoing flight. Any minor updates to the flight plan based on subsequent forecast changes were relayed to the pilots 4 hours before TO, based on 06 UTC day-of-flight forecasts. For the

RF10 and RF 11 example sequence, the actual flight paths flown are shown in Figs 3c and 3d along with the satellite images at the different days of the aircraft operation. This same mission planning procedure was used for all of the 7 flight pairs (dates tabulated in Table 2) that were made during CSET. The detailed flight paths and field reports for each of the mission can be found in the CSET Field Catalog.

The basic flight pattern planned for the low-level sampling segments for all of the flights is shown in Fig. 4. The first segment starts with a descent from the surveying leg at 6 km to about 500 ft. This descent provides a pseudo sounding (aircraft moves horizontally during the 20 k ft descent). Then a level leg is flown at 150 m (500 ft) for about 10 minutes. After this low-level leg the aircraft ascends to about 100 m above the cloud base for another 10 minute leg. During this leg and the 150 m leg, the HCR and the HSRL beams were pointed upward. After the in-cloud leg, the aircraft would do an alternating ascent-descent sequence with a vertical range of about 500 m (1500 ft) to sample cloud top and the stable layer that often caps the cloud. The plan was flexible so that modifications could be made during the aircraft sampling as dictated by local cloud and meteorology conditions.

Mission planning and mission control were done from the Department of Atmospheric Science Department at the University of Washington and the aircraft home base was in Sacramento CA where the EOL flight crew and technicians were located with the airborne mission scientists. Daily mission briefing and planning meetings were held at the University of Washington and networked to facilities at the Sacramento location and to Kona when the aircraft was there.

Flight operations of each mission started with preparation of the aircraft and scientific equipment about 4 hours before TO. The flight crew consisted of two pilots, three technicians onboard the aircraft, the mission scientist and at least one additional scientist/observer. Once airborne, the mission scientist would direct the aircraft sampling sequence during the low-level profile flights and would set the dropsonde points along the surveying parts of the flight. Scientists on the ground could monitor the aircraft operations and view data in near real-time along with GOES satellite products using the satellite-linked Field Catalog and x-chat capabilities. An example of the display from the Field Catalog work space for the midpoint of the RF10 flight on 27 July is shown in Fig. 4b. In this depiction the GV flight path is plotted on the high resolution visible GOES image. Any of the satellite cloud products can be displayed in this same format and selected using a menu that appears on the Field Catalog display. The images from the cameras onboard the G-V can also be viewed at the same time through the web portal to the Field Catalog. The dropsonde points can be plotted on the flight display. During the flight, these Field Catalog near-real time displays can be made using the menu to select the fields to be displayed with the flight track information. In addition the Field Catalog can be to show near-real time displays of time-height plots of the HCR and HSRL returns. Other data collected can be plotted and displayed in real time or after flights using EOL Aeros visualization software.

The playback mode of the Field Catalog allows review of the observations made earlier in the flight or after flight completion. The flight path can be superimposed on the satellite product images. The Field Catalog displays are available to scientists and technicians on the

GV and to anyone on the ground through a standard web connection. Scientists on the ground communicated directly with the mission scientists using x-chat. These real-time exchanges facilitated any modification of the aircraft sampling areas and procedures and made full use of the many eyes that were monitoring the flights and the associated cloud conditions seen from satellite.

4. Observational Highlights

A wide range of boundary layer structures and aerosol, cloud, and precipitation conditions were observed during the CSET missions that captured the cloud system evolution in the Pacific trades. The cloud systems sampled included solid stratocumulus infused with smoke from Canadian wildfires, mesoscale (100-200 km) cloud-precipitation complexes, and patches of shallow cumuli in very clean environments. Ultra clean layers were observed frequently near the top of the boundary layer and were often associated with shallow, veil (optically thin) layered clouds. The extent of aerosol, cloud, drizzle and boundary layer sampling that was made over open areas of the North Pacific along 2-day trajectories during CSET is unprecedented and will enable focused modeling and process studies of cloud system evolution and the role of aerosol-cloud-precipitation interactions in that evolution.

Synoptic conditions during CSET were consistent with normal summertime conditions over the North East Pacific, although sea surface temperatures were above normal. On average the center of the subtropical anticyclone was at about 43 N and 148 E during the observing period (Fig. 5), which is slightly north of the climatological position. Some variations in the strength and location of the anticyclone were observed during the 4 weeks of observations. The sea surface temperatures (Fig. 5) in the study area were about 0.5 °C above 1981-2010 base values. The mean low-level cloudiness from the GOES estimates is shown in Fig. 6. The winds and clouds in the southern parts of the observing areas were occasionally perturbed by tropical storms and cyclones moving through or near this area. But these perturbations had limited impact on the CSET observations.

During CSET a total of 7 two-flight sequences (14 research flights; RF-02 to RF-15; see Table 2) were flown between Sacramento and Kona. Each flight took about 8 hours with about half of this time flown at the beginning and the end of each flight in survey mode at a nominal height of 6 km. The middle of the flight was devoted to the level-leg sampling at low levels and the profiling described previously. Rough estimates of the mean trajectories flown during these 14 flights are shown in Fig. 5 and are overlaid on the mean SST and wind vectors from NCEP reanalyzes. The mean trajectories go from higher lower to higher SSTs with downstream and upstream differences of 4- 8 °C and the mean near-surface winds decreasing in speed and the cloudiness decreases (roughly 80-90% to 40-50 %; Fig. 6).

Sampling areas at the beginning and the ends of individual trajectories for the 14 flights are overlain over the mean cloudiness from the GOES analyses shown in Fig. 6. Most of the initial sampling (blue) areas are in high cloudiness areas relative to the areas at the end points of the trajectories 48-52 hours later. The average cloudiness decreases about 30 % to 50% along each of the couplets. Thus the transition was well sampled on the 14 flights. The locations of the trajectory mapping areas shown in Fig. 6 are listed in Table 2. On the first 6

flights (RF02-RF07) at the beginning of observational period, the low-level sampling time was less than on the flights made after that. Thus, the two sampling areas are specified in Table 2 for RF02-RF07 and three sampling areas are listed for RF08-RF 15 when more time was used for low-level sampling.

a. Lagrangian Evolution Sample

A sample of the Lagrangian tracking of clouds and aerosols with the HCR and HSRL during the outbound RF10 (27 July 2015) and the inbound RF11 (29 July 2011) flight sequences discussed earlier (Fig. 3) are shown in Figs. 7a and 7b. The changes in the boundary layer depth with longitude are shown clearly by the HCR and HSRL returns along the outbound flight in Fig. 7a where the depth increases from about 0.5 km to 1.2 km from 124° to 130° W. From 130° to 137 °W the boundary layer depth is nearly constant at a height of about 1.2 km and then increases to about 2.5 km at 140°W. The cloudiness is substantially reduced west of 140° W.

The boundary layer is more distinctly defined by the lidar than the radar in some cases, since the survey portions of the flight were flown at a height where the radar sensitivity is insufficient to detect low non-precipitating thin clouds. But when flying below the cloud, the lidar is facing upward and does not detect cloud top in optically thick clouds. On the RF11 return flight two days later the boundary layer depth is about 1.8 km from 145 to 135 °W and then decrease from this height to about 300 m at 140 °W.

The low-level sampling legs shown in Fig. 7a and 7b are segmented into the areas labeled by capital letters. The segments labeled on the outbound flight sample the beginning of the trajectories selected for the mission and the corresponding letters on the inbound flight correspond to the equivalent end points of the 48-52 hour trajectories. A blowup of the lidar and the radar sampling made on the BC segments for RF10 and RF11 are shown in Fig. 8. These segments clearly show a strong change in the cloud type and amount between the beginning and the end of the trajectories. After two days there is substantially less low cloud in the end of the trajectory sampling than in the beginning. There is also a notable deepening of the boundary layer from the beginning to the end of the segments. At the beginning of the trajectory sample area BC the radar indicates relative solid cloud cover with drizzle and rain falling from the clouds. The cloud fraction from the remote sensing measurements is about 80%. On the return flight sampling at the end of the BC trajectories, there are relatively few clouds with a few weak echoes from small cumuli. The lidar returns in this area show mesoscale variability in the time-height aerosol structure in the PBL from 0.5 to 1.8 km altitude. This mesoscale variability may be due to processing of the aerosols by previous mesoscale convective activity.

Potential temperature, mixing ratio, and wind profiles at the beginning and the end of the BC trajectory (Fig. 9) show the evolution of the boundary layer structure over the two-day period. As expected, there is substantial warming (about a 4 K increase) and moistening (about 3 g/kg) over the period that are consistent with the increase in SST along the trajectory. The capping inversion defined from the soundings increases from about 1.4 km at the beginning of the trajectory to about 2.3 km at the end. The potential temperature and mixing ratio profiles show some decoupling at the beginning of the trajectory that becomes

more pronounced at the end. Since these profiles represent a combination of vertical and horizontal variability, interpretation of features like the moist layer observed at the top of the boundary layer may be difficult and may reflect mesoscale horizontal variability in the moisture structure as well as the vertical structure.

In total 7 Lagrangian pairs were obtained during CSET and provided an unprecedented description of the evolution of the clouds and boundary layer structures in the North Pacific Trades. Although there was variability on the different days, a common feature was that on the outbound flights the boundary layer was already showing signs of decoupling in the initial sampling areas associated with stratocumulus clouds around 140W. These decoupled stratocumulus areas were followed by areas that were dominated by mesoscale cloud systems. The classic broken fair-weather cumulus fields were not generally sampled on the outbound flights, but were more prevalent on the beginning of the inbound flights originating from Hawaii.

b. Process Studies

The CSET observations also provide an observational basis for underlying processes involved in the evolution of the boundary layer clouds. This included illumination of the role of aerosol-cloud-precipitation interactions and the role of mesoscale cloud systems in the evolution of clouds along the trajectories sampled.

The environments sampled during some of the CSET cases showed substantial variability in the aerosols and associated cloud characteristics. An example of this variability in the extreme is shown for the RF02 (7 July 2015) and RF03(9 July 2015) cases when fires in Canada produced smoke plumes that were advected into the CSET sampling area and impacted clouds in Fig. 10. The effective cloud radius estimates from the GOES satellite products indicate that the boundary layer clouds in the areas are affected by the smoke and showed lower effective radius values compared with those obtained in the cleaner areas to the west of the smoke affected areas. The HSRL returns on the outbound flight RF02 also show substantial aerosol structures above the boundary layer. The *in situ* GV aerosol concentrations (labeled UHSAS in Fig. 10) and mean cloud droplet concentrations sizes (labeled N_D in Fig. 10) obtained on RF02 show much higher aerosol and cloud droplet number concentrations in the eastern part of the low-level sampling areas than those to the west. For a trajectory starting area sampled on the first part of the outbound RF02 flight, the boundary layer UHSAS aerosol concentrations are about 760 cm^{-3} and the concentrations above the boundary layer are about 450 cm^{-3} . In the same air mass sampled on the return flight the boundary layer concentrations are reduced to about 410 cm^{-3} and the above inversion concentrations are about 70 cm^{-3} . But while the boundary layer values are measured in the same air mass, there is no guarantee that the air above the inversion will follow the same trajectory. Regardless, the CSET trajectory analyses are a rich source of information for studying the evolution of aerosols and cloud and precipitation properties in the transition process.

Mesoscale cloud systems in the transition area were common features observed on the CSET flights. An example of the types of systems sampled is shown in Fig. 11. These systems generally have heavy precipitation near the core of the systems with outflow clouds at the

top of the system. The two mesoscale systems sampled with the HSRL and the HCR on the RF07 (19 July 2015) flight have horizontal dimensions of about 20 km and are about 60 km apart. The GOES visible image for the time period when these observations were made is shown in the Fig. 11. Overall the cloud pattern shown in the satellite image can be characterized as open cells like those studied in VOCALS (Wood et al., 2011b). The core of the two systems is characterized by precipitation shafts with relatively high radar reflectivity and downward motions of about 4 ms^{-1} . Clearly defined outflow areas extend from these cores near cloud top. Although the cloud tops in the cores are at a height of about 2 km, the precipitation from these areas can be relatively heavy and of sufficient intensity to give rainbows that were observed from the GV when flying at low levels (example shown in Fig. 11). The precipitation cores of the systems shown in Fig. 11 have a horizontal extent of about 5-10 km horizontally. The out-flow areas in these mesoscale systems by the radar are about double that of the precipitating cloud areas.

The lidar and radar observations made in this case were taken while the GV was flying above the boundary layer. On the edges of the cloud away from the heavily precipitating cloud, the clouds are sufficiently optically thin that aerosols below the cloud can be observed with the HSRL. On the west side of the eastern cloud system two out-flow clouds at different heights are present. Both are sufficiently optically thin that the lidar is able to penetrate both layers in some areas. These types of mesoscale cloud systems were observed on nearly all the CSET flights and clearly indicate that these systems are fundamental to the cloudiness transition observed in the CSET study area. The CSET observations provide a unique data set for studying the heavy precipitation events observed in these clouds and the aerosol-cloud-precipitation interactions involved in these mesoscale complexes.

The mesoscale systems sampled are also rich in different types of aerosol cloud interactions. A feature that was frequently observed during CSET was optically thin veil clouds that were associated with layers of very low aerosol concentrations (UHSAS concentrations $< 10 \text{ # cm}^{-3}$) near the top of the boundary layer. An example of these veil cloud layers and ultra clean layer is shown in Fig. 12 with the HSRL observations made on RF07. A full study of the veil clouds and the clean layers observed during CSET is given in Wood et al. (2018). They estimate that cloud cover associated with the veil clouds to be about 50% within the transition areas sampled during CSET. These clouds are both physically and optically thin. In addition, to the extensive lidar and radar observations during CSET, the GV made several direct penetrations of the veil clouds during CSET that allowed for a characterization of the properties of the clouds and the aerosols in the vicinity of the clouds.

The clean layers near cloud top are clearly shown on several of the flights (Wood et al, 2018). For example, the UHSAS aerosol concentrations measured on the outbound RF 06 (7 July) and inbound RF 07 (9 July) are shown in Fig. 13. On the inbound flight there is a well-defined area of very low aerosol concentrations near the mean tops of clouds. The veil clouds and clean layers observed appear to be closely coupled to the mesoscale cloud systems like those shown in Fig. 11. A challenge will be to fully understand how the gray clouds form and their connection to the clean layers. Modeling studies in progress are working to address these questions.

This section is intended to give a snapshot of some of the observations made during CSET. The CSET observations and the flights that were flown can be explored further by visiting the CEST Field Catalog.

5. Summary

CSET made substantial advancement in our characterization of the evolution of cloud systems along the southeast extent of the Pacific anticyclone further CET and demonstrated the utility of a Lagrangian sampling strategy. The observations provide a unique opportunity to study of the processes involved in the cloud system evolution in the Pacific trades and to characterize that evolution in a way that can be used to evaluate model simulations of the evolutions. CSET demonstrated the feasibility of a Lagrangian sampling strategy with NSF/NCAR GV aircraft to study cloud system evolution. The range, endurance, and observational capabilities of the GV make it an ideal tool for studying shallow boundary layer clouds and mesoscale cloud systems over large domains. The HCR and HSRL remote sensing capabilities on the GV were critical to the success of CSET. They provided a detailed characterization of the structure of both precipitating and non-precipitating clouds and the aerosol distributions above, below and around clouds. CSET provided unprecedented observations of the evolution of boundary layer structure and cloud and aerosol fields that will provide several cases for model evaluation and development. Extensive cloud areas were sampled and then resampled 48 hrs later along trajectories between California and Hawaii on 7 round-trip missions involving low-level flights. These observations and subsequent characterizations of cloud and boundary layer evolution along the trajectories provide an unprecedented data set for evaluating cloud system evolution in several classes of models.

The observing strategy employed allowed for a low-level sampling of clouds over a total flight distance of about 20,000 km and another 20,000 km of sampling made in survey mode where the radar and lidar were used to characterize clouds in the boundary layer and dropsondes were used to define boundary layer structure. Extensive observations of key features of cloud system evolution were made—mesoscale precipitating cloud complexes, gray cloud layers, and ultra clean layers at boundary layer top in areas far removed from areas sampled on past aircraft missions.

This project demonstrated the power of EOL Field Catalog II for mission planning, flight operations, and data archiving. Further, the Catalog provided enhanced learning and teaching experiences for the undergraduate and graduate students involved directly in CSET. Although the restricted passenger space on the GV limited the number of students who could actually fly on missions, the Field Catalog allowed students to follow the progress of the CSET flights in real time and examine the data as they were downloaded from the aircraft. The CSET Field Catalog continues to contribute to classroom teaching and learning activities for both undergraduate and graduate world-wide. A CSET teaching module was developed (<https://www.eol.ucar.edu/content/cset-educational-module>; <http://cseteducation.weebly.com/>) that allows students to experience the activities involved in carrying out a major aircraft field deployment like CSET. This module makes heavy use of EOL's CSET Field Catalog (<http://catalog.eol.ucar.edu/cset>) in playback mode (using the

EOL Field Catalog Maps application) and uses GV observations for analysis exercises that can be completed by the students. The module endeavors to have students experience the types of activities involved in the field program and includes mission planning exercises. This module can also serve as a model for future EOL related aircraft field missions.

In summary, CSET made substantial advancement in our characterization of the evolution of cloud systems along the southeast extent of the North Pacific anticyclone. The observations will serve as a unique source of information for many future process and modeling studies that will lead ultimately to improved simulations of low-level clouds in global models. The observational techniques developed and demonstrated using the NSF/NCAR GV as an observing platform provides a firm basis for future studies of boundary layer cloud regimes using the GV.

Acknowledgments:

A special note of thanks and appreciation goes to NCAR Earth Observing System staff supporting CSET for their efforts and support in the field. A special thanks to the GV pilots who worked diligently to accommodate our needs to make the Lagrangian flight missions possible. This research was supported by the National Science Foundation Grant AGS-1445832 to the University of Miami, Grant AGS-1445813 to the University of Washington, and Grant AGS-1445831 to the University of Chicago V.G. was also supported by the U.S. Department of Energy's (DOE) Atmospheric System Research (ASR), an Office of Science, Office of Biological and Environmental Research (BER) program, under contract DE-AC02-06CH11357 awarded to Argonne National Laboratory. We gratefully acknowledge the computing resources provided on Blues, a high-performance computing cluster operated by the Laboratory Computing Resource Center at Argonne National Laboratory. The National Center for Atmospheric Research is funded by the National Science Foundation. NCEP Reanalysis data were provided by the NOAA/OAR/ESRL PSD, Boulder, Colorado, USA, from their Web site at <https://www.esrl.noaa.gov/psd/>

References

- Ackerman AS, Kirkpatrick MP, Stevens DE, and Toon OB, 2004: The impact of humidity above stratiform clouds on indirect aerosol climate forcing. *Nature*, 432, 1014–1017. [PubMed: 15616559]
- Albrecht BA, Jensen MP, and Syrett WJ, 1995: Marine boundary layer structure and fractional cloudiness. *J. Geophys. Res.*, 100, 14209–14222.
- Albrecht BA, Bretherton CS, Johnson D, Schubert WH, Shelby Frisch A, 1995: The Atlantic Stratocumulus Transition Experiment – ASTEX. *Bull. Amer. Meteor. Soc.*, 76, p. 889–904.
- Berner AH, Bretherton CS, and Wood R, 2011: Large-eddy simulation of mesoscale dynamics and entrainment around a pocket of open cells observed in VOCALS RF06. *Atmos. Chem. Phys.*, 11, 10525–10540.
- Berner AH, Bretherton CS, and Wood R, 2011: Large-eddy simulation of mesoscale dynamics and entrainment around a pocket of open cells observed in VOCALS RF06. *Atmos. Chem. Phys.*, 11, 10525–10540.
- Berner AH, Bretherton CS, Wood R, and Muhlbauer A 2013: Marine boundary layer cloud regimes and POC formation in an LES coupled to a bulk aerosol scheme. *Atmos. Chem. Phys.*, 13, 12549–12572, 2013.
- Blossey PN, Bretherton CS, Zhang M, Cheng A, Endo S, Heus T, Liu Y, Lock A, de Roode SR, and Xu KM (2013), Sensitivity of marine low clouds to an idealized climate change: The CGILS LES intercomparison, *J. Adv. Model. Earth Sys.*, doi:10.1002/jame.20025.
- Bony S and Dufresne JL, 2005: Marine boundary layer clouds at the heart of tropical cloud feedback uncertainties in climate models. *Geophys. Res. Lett.* 32, L20806.
- Bretherton CS and Pincus R, 1995: Cloudiness and Marine Boundary Layer Dynamics in the ASTEX Lagrangian Experiments. Part I: Synoptic setting and vertical structure. *J. Atmos. Sci.*, 52, 2707–2723.

- Bretherton CS, Austin PA and Siems ST, 1995: Cloudiness and Marine Boundary Layer Dynamics in the ASTEX Lagrangian Experiments. Part II: Cloudiness, drizzle, surface fluxes and entrainment. *J. Atmos. Sci*, 52, 2724–2735.
- Bretherton CS, and Wyant MC, 1997: Moisture transport, lower tropospheric stability and decoupling of cloud-topped boundary layers. *J. Atmos. Sci* 54, 148–167.
- Bretherton CS, Krueger SK, Wyant MC, Bechtold P, Van Meijgaard E, Stevens B, and Teixeira J, 1999: A GCSS boundary-layer cloud model intercomparison study of the First ASTEX Lagrangian Experiment. *Bound-Lay. Meteorol* 93, 341–380.
- Bretherton CS, Blossey PN, and Uchida J, 2007: Cloud droplet sedimentation, entrainment efficiency, and subtropical stratocumulus albedo. *Geophys. Res. Lett*, 34, L03813, doi: 10.1029/2006GL027648.
- Bretherton CS, Uchida J, and Blossey PN, 2010a: Slow manifolds and multiple equilibria in stratocumulus-capped boundary layers. *Journal of Advancing Modeling Earth Systems*, 2, Art.#14, 20 pp.
- Bretherton CS, Wood R, George RC, Leon D, Allen G, and Zheng X, 2010b: Southeast Pacific stratocumulus clouds, precipitation and boundary layer structure sampled along 20 S during VOCALS-REx, *Atmos. Chem. Phys*, 10, 15921–15962.
- Bretherton CS, Blossey PN, and Jones CR (2013), Mechanisms of marine low cloud sensitivity to idealized climate perturbations: A single-LES exploration extending the CGILS cases, *J. Adv. Model. Earth Syst*, 5, 316–337, doi:10.1002/jame.20019.
- Brost RA, Lenschow DH, Wyngaard JC, 1982a: Marine stratocumulus layers. Part 1: Mean conditions. *J. Atmos. Sci*, 39, 800–817.
- Brost RA, Wyngaard JC, Lenschow DH, 1982b: Marine stratocumulus layers. Part II: Turbulence budgets. *J. Atmos. Sci*, 39, 818–836.
- Caldwell P, and Bretherton CS, 2009: Large eddy simulation of the diurnal cycle in Southeast Pacific stratocumulus. *J. Atmos. Sci*, 66, 432–449.
- Fang M, Albrecht B, Jung E, Kollias P, Jonsson H, and PopStefanija I, 2017: Retrieval of Vertical Air Motion in Precipitating Clouds Using Mie Scattering and Comparison with In Situ Measurements. *J. Appl. Meteor. Climatol*, 56, 537–553.
- Fugal JP, and Shaw RA, 2009: Cloud particle size distributions measured with an airborne digital in-line holographic instrument. *Atmos. Meas. Tech. Discuss*, 2, 659–688, doi:10.5194/amtd-2-659-2009.
- Geerts B and Miao Q, 2005: The use of millimeter Doppler radar echoes to estimate vertical air velocities in the fair-weather convective boundary layer. *J. Atmos. Oceanic Technol*, 22, 225–246.
- Gerber H, Frick G, Jensen JB and Hudson JG, 2008: Entrainment, mixing, and microphysics in trade-wind cumulus, *J. Meteorol. Soc. Japan*, 86A, 87–106.
- Ghate VP, Albrecht BA and Kollias P, 2010: Vertical velocity structure of non-precipitating continental boundary layer stratocumulus clouds. *J. Geophys. Res*, 115, D13204, doi: 10.1029/2009JD013091
- Ghate VP, Miller MA and DiPretore L, 2011: Vertical velocity structure of marine boundary layer trade wind cumulus clouds. *J. Geophys. Res*, 115, D23201, doi: 10.1029/2010JD015344
- Giangrande SE, Luke EP and Kollias P, 2012: Characterization of vertical velocity and drop size distribution parameters in widespread precipitation at ARM facilities. *J. Appl. Meteor. Climatol*, 51, 380–391.
- Glienke S, Kostinski A, Fugal J, Shaw RA, Borrmann S, and Stith J, 2017: Cloud droplets to drizzle: Contribution of transition drops to microphysical and optical properties of marine stratocumulus clouds. *Geophys. Res. Lett*, 44, 8002–8010, doi: 10.1002/2017GL074430.
- Hartmann DL and Short D, 1980: On the use of earth radiation budget statistics for studies of clouds and climate. *J. Atmos. Sci*, 37, 1233–1250.
- Hartmann, Ockert M and Michelson M, 1992: the effect of cloud type on the earth's energy balance. *J. Clim* 5 1281–1304.
- Jung E, Albrecht BA, Feingold G, Jonsson HH, Chuang P, and Donaher SL: Aerosols, clouds, and precipitation in the North Atlantic trades observed during the Barbados aerosol cloud experiment – Part 1: Distributions and variability, *Atmos. Chem. Phys*, 16, 8643–8666, doi:10.5194/acp-16-8643-2016.

- Kalnay E, Kanamitsu M, Kistler R, Collins W, Deaven D, Gandin L, Iredell M, Saha S, White G, Woollen J, Zhu Y, Chelliah M, Ebisuzaki W, Higgins W, Janowiak J, Mo KC, Ropelewski C, Wang J, Leetmaa A, Reynolds R, Jenne R, and Joseph D, 1996: The NCEP/NCAR 40-Year Reanalysis Project. *Bull. Amer. Meteor. Soc.*, 77, 437–472, 10.1175/1520-0477(1996)077<0437:TNYRP>2.0.CO;2
- Kazil J, Wang H, Feingold G, Clarke AD, Snider JR, and Bandy AR, 2011: Chemical and aerosol processes in the transition from closed to open cells during VOCALS-REx, *Atmos. Chem. Phys. Discuss.*, 11, 4687–4748, doi:10.5194/acpd-11-4687-2011, 2011.
- Klein SA, and Hartmann DL, 1993: The seasonal cycle of low stratiform clouds. *J. Climate*, 6, 1588–1606.
- Klein S, Hartmann D and Norris J, 1995: On the relationships among low-cloud structure, sea surface temperature and atmospheric circulation in the summertime northeast Pacific. *J. Climate*, 8, p. 1140–115.
- Kollias P, Albrecht BA and Marks F Jr. 2000: Why Mie? Accurate observations of vertical air velocities and raindrops using a cloud radar. *Bull. Amer. Meteor. Soc.*, 83, 1471–1483.
- Kollias P, Szyrmer W, Rémillard J, and Luke E 2011: Cloud radar Doppler spectra in drizzling stratiform clouds: 2. Observations and microphysical modeling of drizzle evolution, *J. Geophys. Res.*, 116, D13203, doi:10.1029/2010JD015238.
- Lilly DK, 1968: Models of cloud topped mixed layers under a strong inversion. *Quart. J. Roy. Meteor. Soc.* 94, 292–309.
- Lothon M, Lenschow DH, Leon D and Vali G, 2004: Turbulence measurements in marine stratocumulus with airborne Doppler radar. *Quart. J. Roy. Meteor. Soc.*, 131, 2063–2080
- Luke EP and Kollias P, 2013: Separating Cloud and Drizzle Radar Moments during Precipitation Onset Using Doppler Spectra. *J. Atmos. Oceanic Technol.*, 30, 1656–1671, 10.1175/JTECH-D-11-00195.1.
- McGibbon J and Bretherton CS, 2017: Skill of ship-following large-eddy simulations in reproducing MAGIC observations across the northeast Pacific stratocumulus to cumulus transition region, *Journal of Advances in Modeling Earth Systems*, 2017, 9, 2, 810.
- Mechoso CR, Wood R, Weller R, Bretherton CS, Clarke AD, Coe H, Fairall C, Farrar JT, Feingold G, Garreaud R, Grados C, McWilliams JC, de Szoeke SP, Yuter SE, and Zuidema P 2014: Ocean-Cloud-Atmosphere-Land Interactions in the Southeastern Pacific: The VOCALS Program. *Bull. Amer. Meteorol. Soc.*, 95, 357–37, 2014.
- Mellado JP, 2010 The evaporatively-driven cloud-top mixing layer.. *J. Fluid. Mech* 660, 5–36.
- Miller MA, and Albrecht BA, 1995: Surface-Based Observations of Mesoscale Cumulus Stratocumulus Interaction during ASTEX. *J. Atmos. Sci.*, 52 (16), 2809–2826.
- Minnis P, et al. (2008), Near-real time cloud retrievals from operational and research meteorological satellites, *Proc. SPIE Int. Soc. Opt. Eng.*, 7107, 710703, doi:10.1117/12.800344.is.etal.SPIE.abs.08.pdf.
- Minor HA, Rauber RM, Göke S, Di Girolamo L, 2011: Trade wind cloud evolution observed by polarization radar: Relationship to giant condensation nuclei concentrations and cloud organization. *J. Atmos. Sci.*, 68, 1075–1096.
- Morley B, Spuler S, Vivekanandan J, Hayman M, Eloranta E, 2012: Airborne and ground-based measurements with the NCAR's GVHSRL. 16th International Symposium for the Advancement of Boundary-layer Remote Sensing, Boulder CO.
- O'Connor EJ, Hogan RJ, and Illingworth AJ, 2005: Retrieving Stratocumulus Drizzle Parameters Using Doppler Radar and Lidar. *J. Appl. Meteor.*, 44, 14–27, 10.1175/JAM-2181.1
- Neggers R, Neelin D and Stevens B, 2007: Impact mechanisms of shallow cumulus convection on the tropical dynamics. *J. Climate*, 20, 2623–2642.
- Norris JR, 1998: Low cloud type over the ocean from surface observations. Part I: relationship to surface meteorology and the vertical distribution of temperature and moisture. *J. Climate*, 11, 369–382
- Nuijens L, Stevens B, and Siebesma AP, 2009: The environment of precipitating shallow cumulus convection. *J. Atmos. Sci.*, 66, 1962–1979.

- Painemal D and Zuidema P, 2013: The first aerosol indirect effect quantified through airborne remote sensing during VOCALS-Rex. *Atmos Chem. Phys.* 13, pp. 917–931. doi: 10.5194/acp-13-917-2013.
- Rauber RM, and Coauthors, 2007: Rain in shallow cumulus over the ocean: The RICO campaign. *Bull. Amer. Meteor. Soc.* 88, 1912–1928.
- Rauber RM, Ellis SM, Vivekanandan J, Stith J, Lee W, McFarquhar GM, Jewett BF, and Janiszewski A, 2017: Finescale Structure of a Snowstorm over the Northeastern United States: A First Look at High-Resolution HIAPER Cloud Radar Observations. *Bull. Amer. Meteor. Soc.* 98, 253–269, doi: 10.1175/BAMS-D-15-00180.1.
- Razenkov IA, Eloranta EW, Hedrick JP, Holz RE, Kuehn RE and Garcia JP, 2002: A High Spectral Resolution Lidar Designed for Unattended Operation in the Arctic, 21st International Laser Radar Conference}, July 8-12, 2002, Quebec, Canada.
- Sandu I, and Stevens B, 2011: On the factors modulating the stratocumulus to cumulus transitions. *J. Atmos. Sci.* in press, doi: 10.1175/2011JAS3614.1
- Schwartz MC, Ghate VP, Cadetdu M, Vivekanandan J, Ellis S, Tsai P, Eloranta E, Albrecht B, Zuidema P, Wood R and Bretherton CS: Merged Cloud and Precipitation Dataset from the HIAPER-GV for the Cloud System Evolution in the Trades (CSET) campaign. (In preparation).
- Spuler SM, and Fugal JP, 2011: Design of an in-line, digital holographic imaging system for airborne measurement of clouds. *Appl. Opt.* 50, 1405–1412, doi:10.1364/AO.50.001405. [PubMed: 21460907]
- Sun-Mack S, Minnis P, Chen Y, Kato S, Yi Y, Gibson S, Heck PW, and Winker D, 2014: Regional apparent boundary layer lapse rates determined from CALIPSO and MODIS data for cloud height determination. *J. Appl. Meteorol. Climatol.* 53, 990–1011, doi:10.1175/JAMC-D-13-081.1.
- Soden BJ, and Vecchi GA, 2011: The vertical distribution of cloud feedback in coupled ocean-atmosphere models. *Geophys. Res. Lett.* doi: 10.1029/2011GL047632
- Stevens B, Duan J, McWilliams JC, Munnich M and Neelin JD, 2002: Entrainment, Rayleigh friction and boundary layer winds over the tropical Pacific. *J. Climate*, 15, 30–44.
- Stevens B, and coauthors, 2003: Dynamics and Chemistry of Marine Stratocumulus: DYCOMS-II. *Bull. Amer. Meteorol. Soc.* 84, 579–593.
- Teixeira J, and co-authors, 2011: Tropical and sub-tropical cloud transitions in weather and climate prediction models: The GCS/WGNE Pacific cross-section intercomparison (GPCI). *J. Climate*, 24, 5223–5256.
- Terai CR, Wood R, Leon DC, and Zuidema P, 2012: Does precipitation susceptibility vary with increasing cloud thickness in marine stratocumulus?, *Atmos. Chem. Phys.* 12, 4567–4583, doi: 10.5194/acp-12-4567-2012.
- Tiedtke M, 1989: A comprehensive mass flux scheme for cumulus parameterization in large-scale models. *Mon. Wea. Rev.* 117, 1779–1800.
- Ulaby FT, Moore RK, and Fung AK, 1981: *Microwave Remote Sensing: Active and Passive*, Vol. I -- *Microwave Remote Sensing Fundamentals and Radiometry*, Addison-Wesley, Advanced Book Program, Reading, Massachusetts, 456 pp.
- van der Dussen JJ, and coauthors, 2013: The GASS/EUCLIPSE Model Intercomparison of the Stratocumulus Transition as Observed During ASTEX: LES results. *J. Adv. Model. Earth Syst.* submitted 11/2012.
- Vivekanandan J, and Coauthors, 2015: A wing pod-based millimeter wavelength airborne cloud radar. *Geoscientific Instrumentation, Methods and Data Systems*, 5, 117–159, doi:10.5194/gid-5-117-2015.
- Wang H, Feingold G, Wood R, and Kazil J, 2010: Modelling microphysical and meteorological controls on precipitation and cloud cellular structures in Southeast Pacific stratocumulus, *Atmos. Chem. Phys.* 10, 6347–6362, doi:10.5194/acp-10-6347-2010.
- Wang Y and Geerts B, 2012: Composite vertical structure of vertical velocity in non-precipitating cumulus clouds. *Mon. Weath. Rev.* Early Online Release.
- Wood R, 2005: Drizzle in stratiform boundary layer clouds, part I: Vertical and horizontal structure. *J. Atmos. Sci.* 62, 3011–3033.

- Wood R, 2007: Cancellation of aerosol indirect effects in marine stratocumulus through cloud thinning. *J. Atmos. Sci.*, 64, 2657–2669.
- Wood R, Bretherton CS, and 32 coauthors, 2011a: The VAMOS Ocean-Cloud-Atmosphere-Land Study Regional Experiment (VOCALS-REx): goals, platforms, and field operations. *Atmos. Chem. Phys.*, 11, 627–654.
- Wood R, Bretherton CS, Leon D, Clarke AD, Zuidema P, Allen G, and Coe H, 2011b: An aircraft case study of the spatial transition from closed to open mesoscale cellular convection over the Southeast Pacific. *Atmos. Chem. Phys.*, 11, 2341–2370.
- Wood R, 2012: Stratocumulus clouds. *Mon. Wea. Rev.*, 140, 2373–2423.
- Wood R Kuan-Ting O, Bretherton C, Mohrmann J, Albrecht BA, Zuidema P, Ghate V, Schwartz C, Eloranta E, Glienke S, Shaw R, Fugal J, Minnis P, 2018: Ultraclean layers and optically thin clouds in the stratocumulus to cumulus transition: Part I. Observations. *J. Atmos. Sci.* (in press).
- Wyant MC, Bretherton CS, Rand HA, and Stevens DE, 1997: Numerical simulations and a conceptual model of the stratocumulus to trade cumulus transition. *J. Atmos. Sci.* 54, 168–192.
- Wyant MC, Wood R, Bretherton CS, Mechoso, and 16 coauthors, 2010: The PreVOCA experiment: modeling the lower troposphere in the Southeast Pacific, *Atmos. Chem. Phys.*, 10, 4757–4774, doi: 10.5194/acp-10-4757-2010.
- Zhang MH and co-authors, 2005: Comparing clouds and their seasonal variations in 10 atmospheric general circulation models with satellite measurements. *J. Geophys. Res.*, 110, D15S02, doi: 10.1029/2004JD005021
- Zhou X, Kollias P, and Lewis ER (2015), Clouds, precipitation and marine boundary layer structure during the MAGIC Field Campaign, *J. Clim.*, 28, 2420–2442, doi: 10.1175/JCLI-D-14-00320.1.
- Zuidema P, Li Z, Hill R, Bariteau L, Rilling B, Fairall C, Brewer WA, Albrecht B and Hare J, 2012a: On trade-wind cumulus cold pools. *J. Atmos. Sci.*, 69, pp. 258–277, doi: 10.1175/jas-d-11-0143.1
- Zuidema P, Leon D, Pazmany A and Cadeddu M, 2012b: Aircraft millimeter-wave passive sensing of cloud liquid water and water vapor during VOCALS-REx. *Atmos. Chem. Phys.*, 12, pp. 355–369, doi:10.5194/acp-12-355-2012.



Figure 1: NSF/NCAR G-V and visible GOES satellite image with aircraft path and winds on flight made on 27 July 2015 (RF07) during CSET. The blue points indicate where dropsonde launches made. Photos were taken during CSET GV flights and show clouds observed along CSET varying in the downstream direction (east to west) from solid stratus (right bottom photo) to mesoscale complexes to fair-weather cumuli (left bottom photo).



Figure 2:
Photos of HCR on wing of GV and HSRL pointing up and down inside the GV.

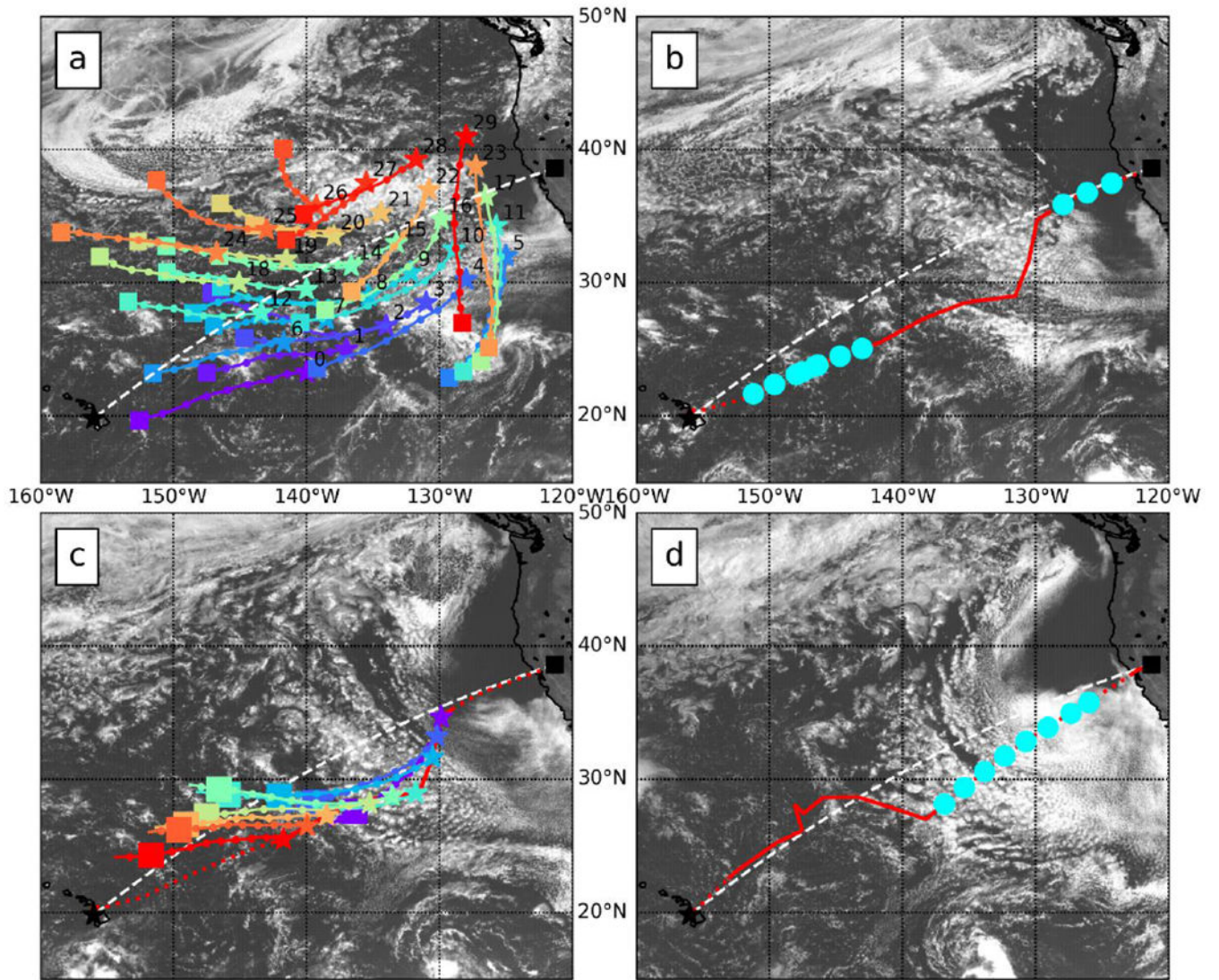


Figure 3:

Visible satellite images with trajectories used for mission planning and flight operations. White dotted line indicates great circle from Sacramento, CA to Kona, HI. a) Trajectory swarm used on 26 June 2015 for RF-10 flight planning, with GOES visible imagery from the morning of June 26; b) RF-10 flight path with dropsonde locations marked by closed circles, GOES visible imagery from morning of June 27 (day of flight); c) RF10 flight path and RF11 planning trajectories (return flight planned through squares at trajectory ends), GOES visible imagery from morning of June 28 (day between flights); d) return flight path flown for RF-11 with dropsonde locations, GOES visible imagery for June 29 (day of return flight).

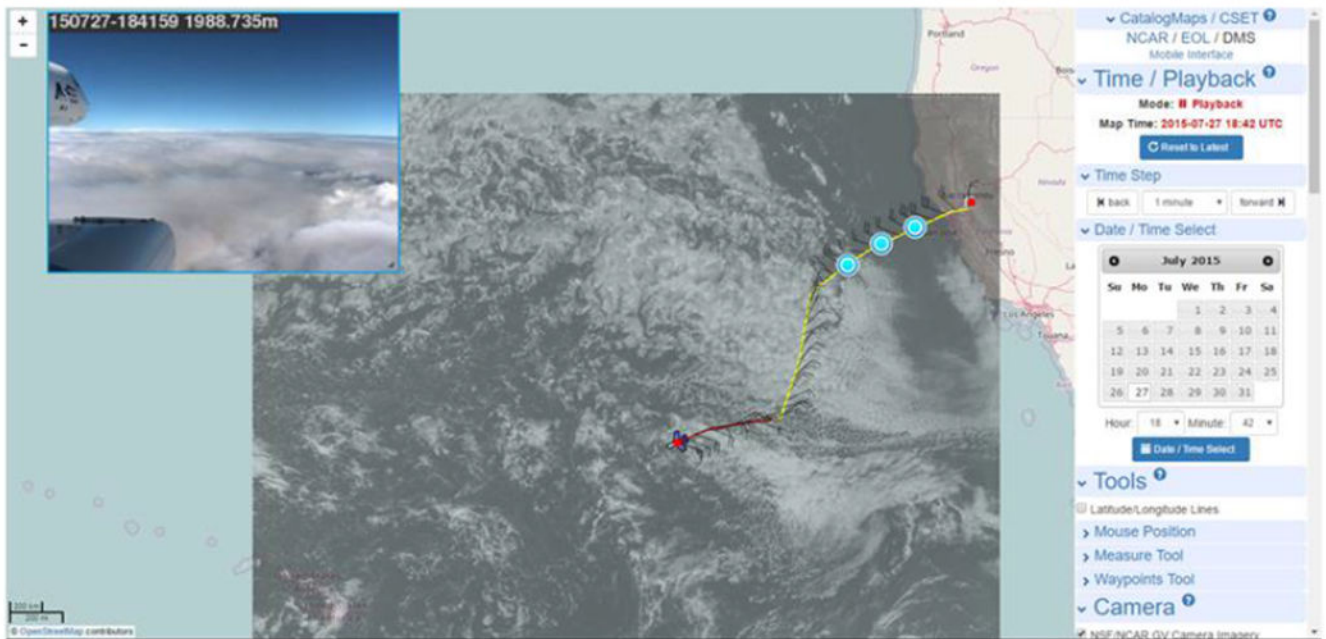
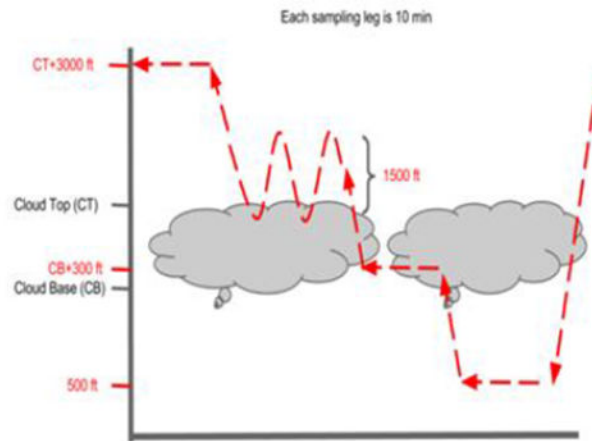


Figure 4:

a) Flight pattern plan for low-level sampling legs. Level legs are typically 8-10 minutes in duration. b) Screen shot of display from EOL Field Catalog II during RF 10; 27 July 2015 at 1042 UTC. Yellow line shows flight path with wind barbs overlain on high resolution visible GOES image and real-time photo from camera mounted on starboard (right) wing of GV.

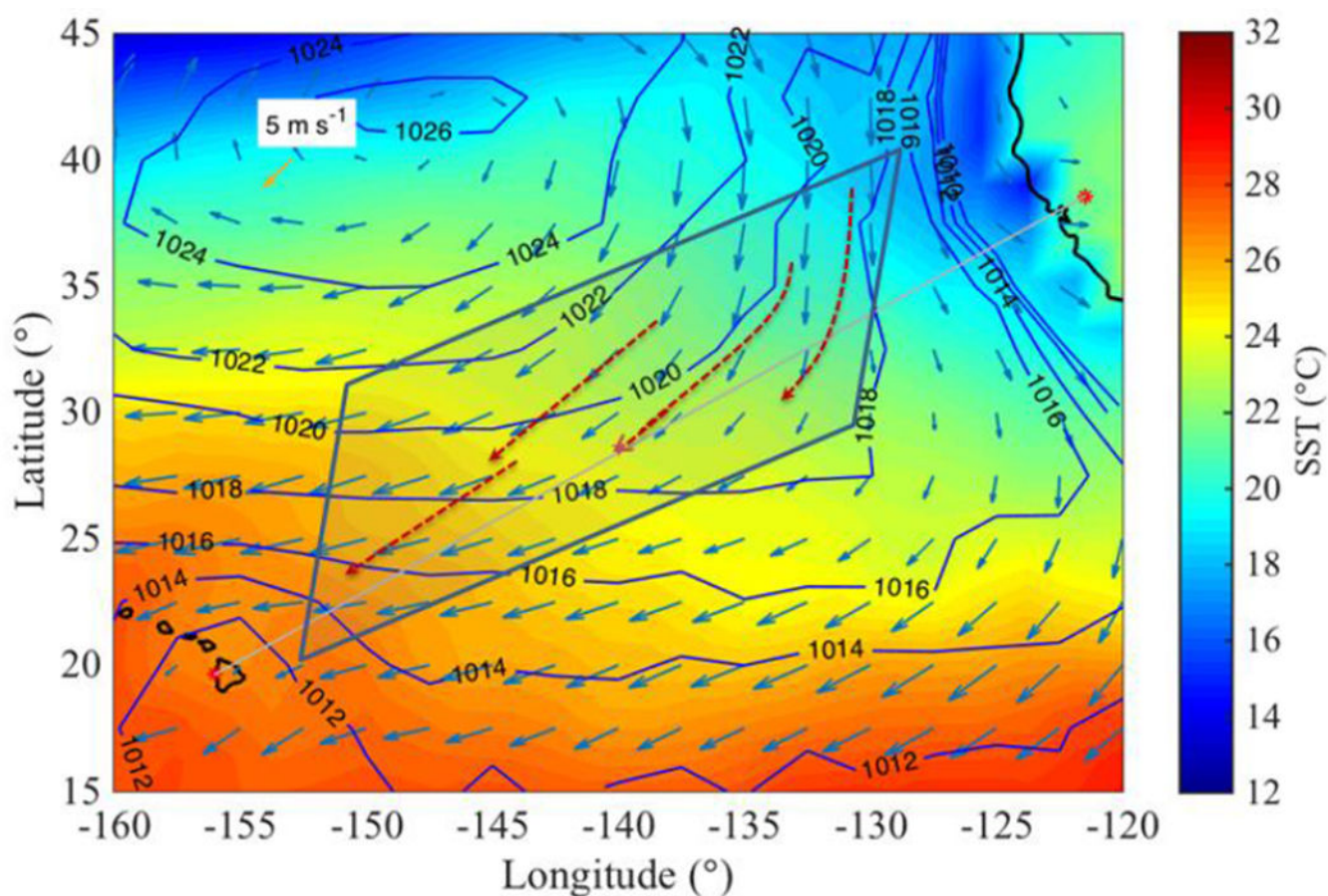


Figure 5:
Mean surface pressure, SST, and surface wind vectors for CSET (July 6-August 12) from NCAR/NCEP Reanalysis (Kalany et al. 1996). Study area is indicated by shaded areas and trajectories represent rough means of all trajectories flown.

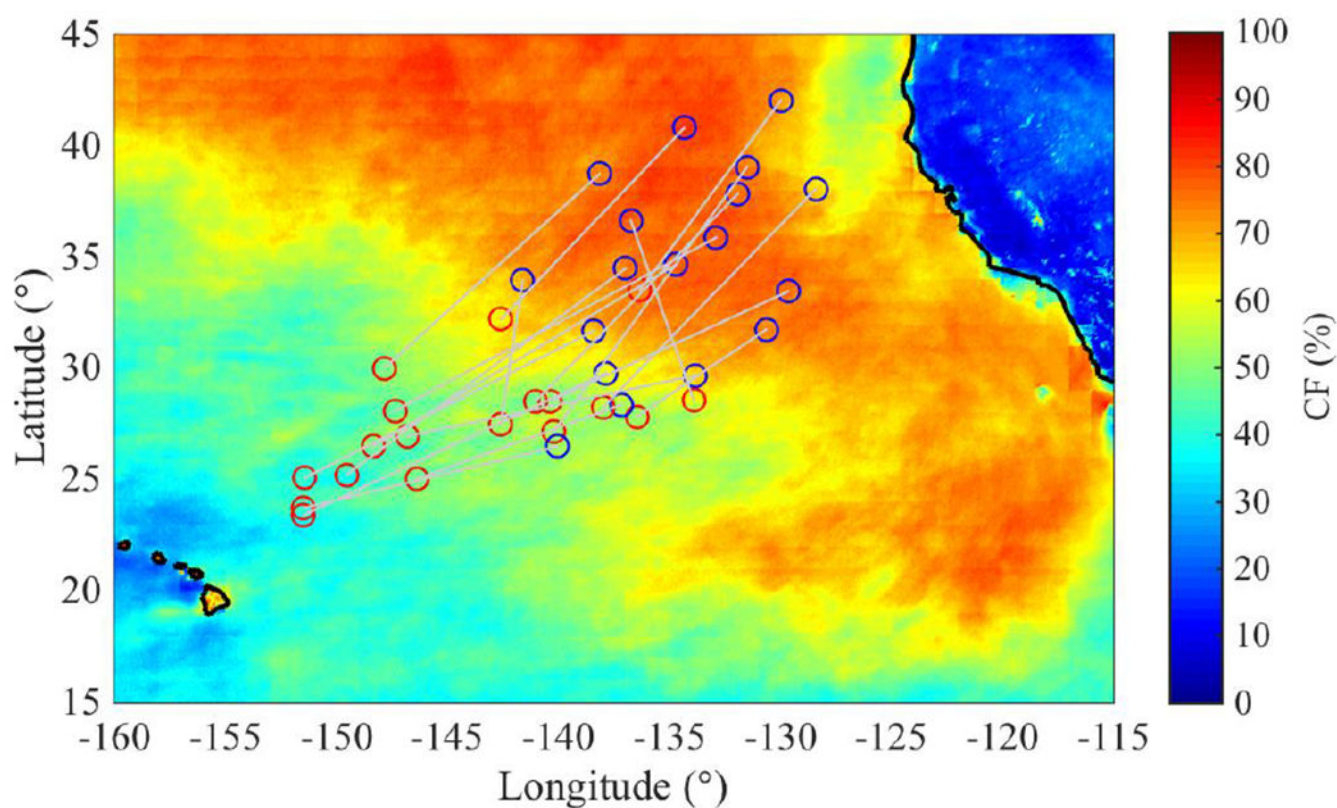


Figure 6:

Cloud fraction from GOES analyses (using Minnis et al, 2008). Blue points are starting points of trajectory sampling areas on outbound flights from Sacramento. Red points are areas sampled at end points of 48-52 hr. trajectories.

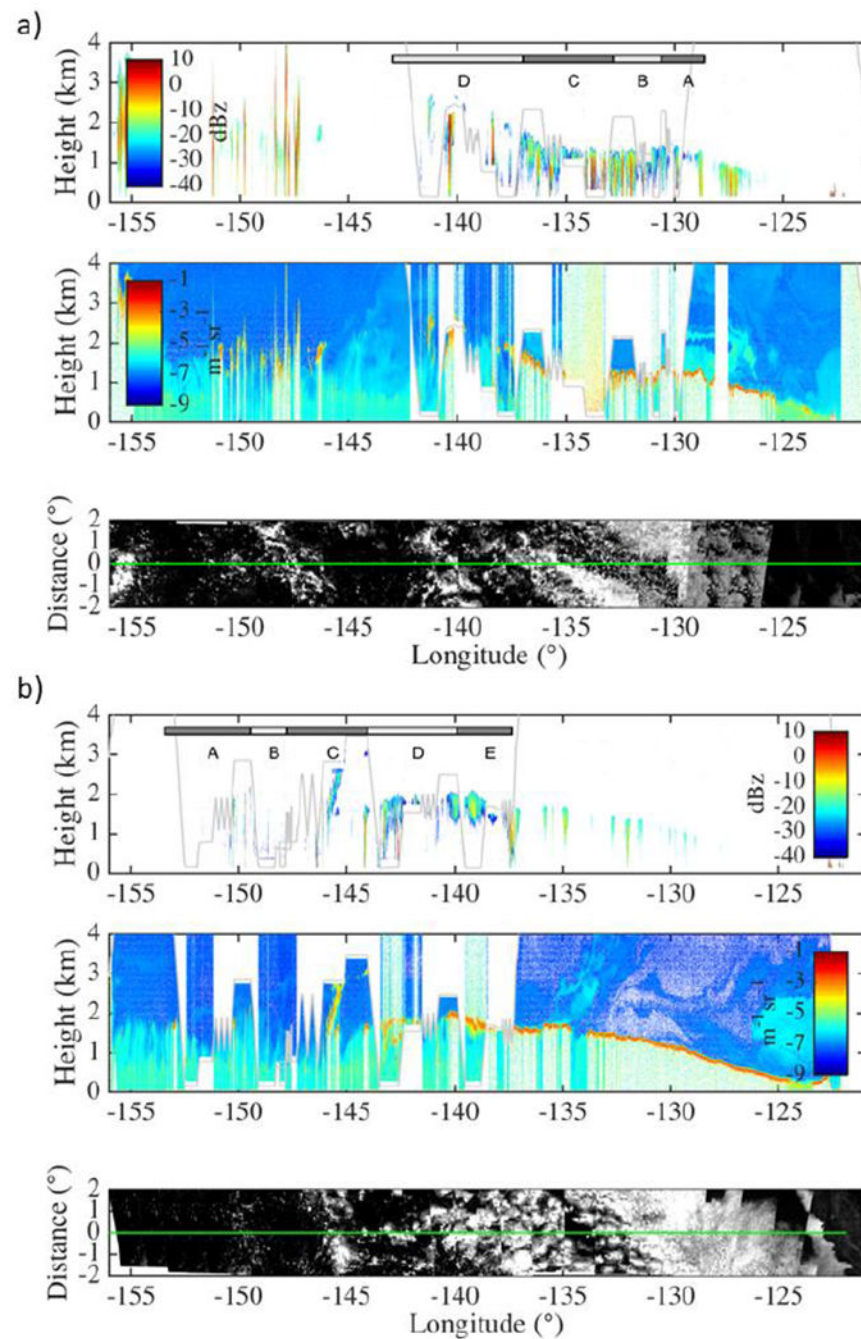
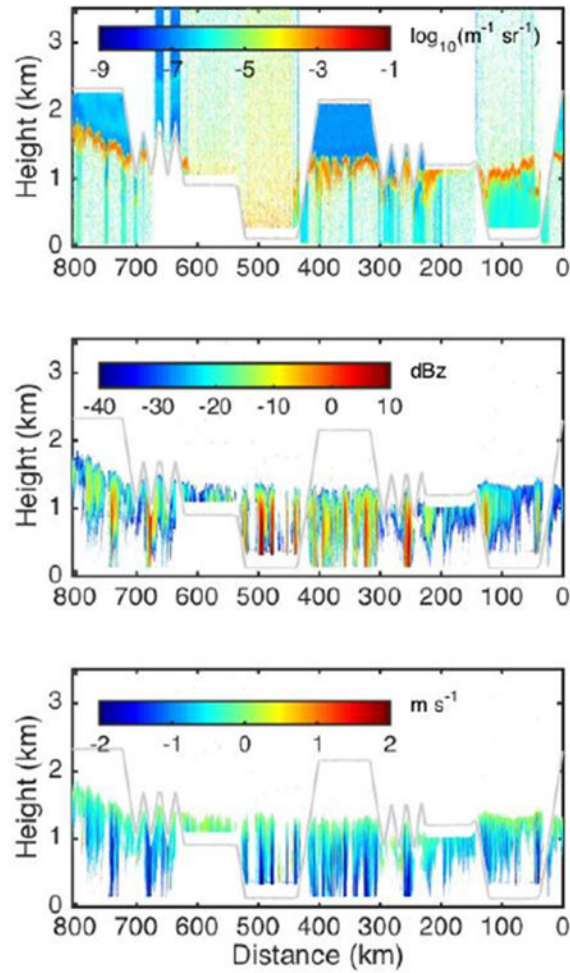


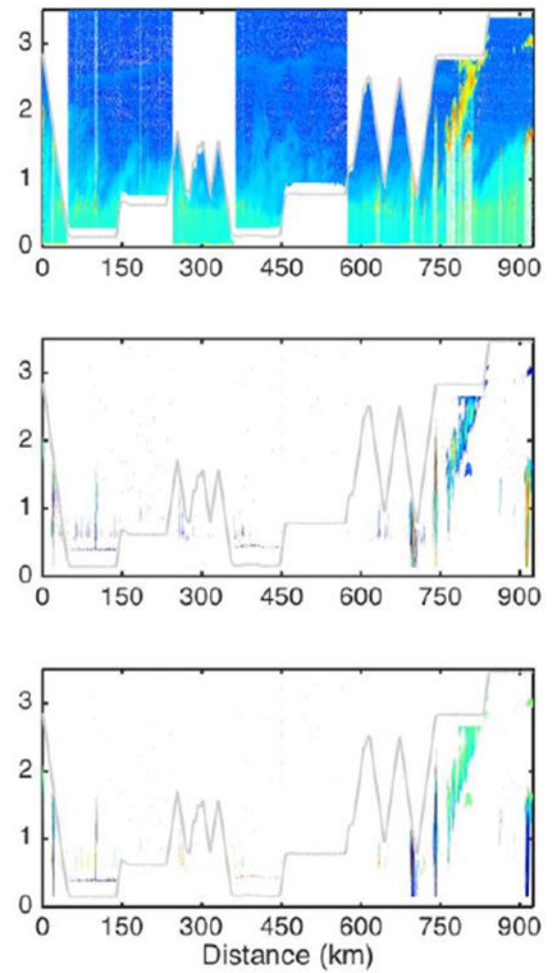
Figure 7:

HSRL and HCR returns for RF 10 (27 July 2010) shown as a function of longitude with corresponding high resolution visible GOES images ($4^\circ \times 4^\circ$ sample areas) stitched together. The lettered areas indicate the box areas analyzed at the trajectory starting points. Since flights were not made in a strictly east-west orientation, the data plotted on the longitudinal axes can be relatively compressed during parts of the flight where there might be a strong north-south component to the flight path. b) for inbound RF-11 (July 29 2010).

a)



b)

**Figure 8:**

HSRL backscatter with HCR reflectivity and Doppler velocity for a) RF-10 segments BC at beginning of trajectories and b) RF-11 segments BC at trajectory end points.

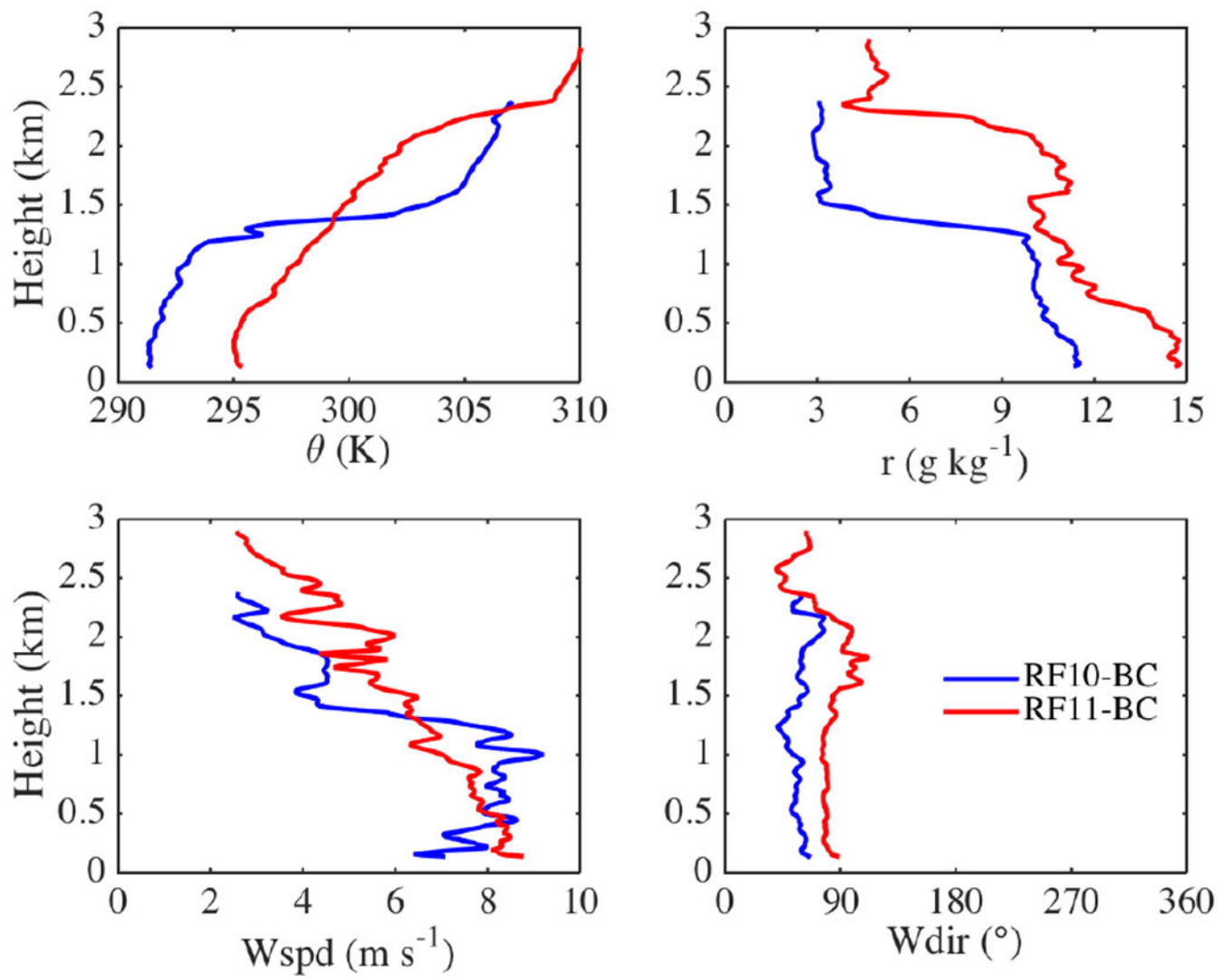
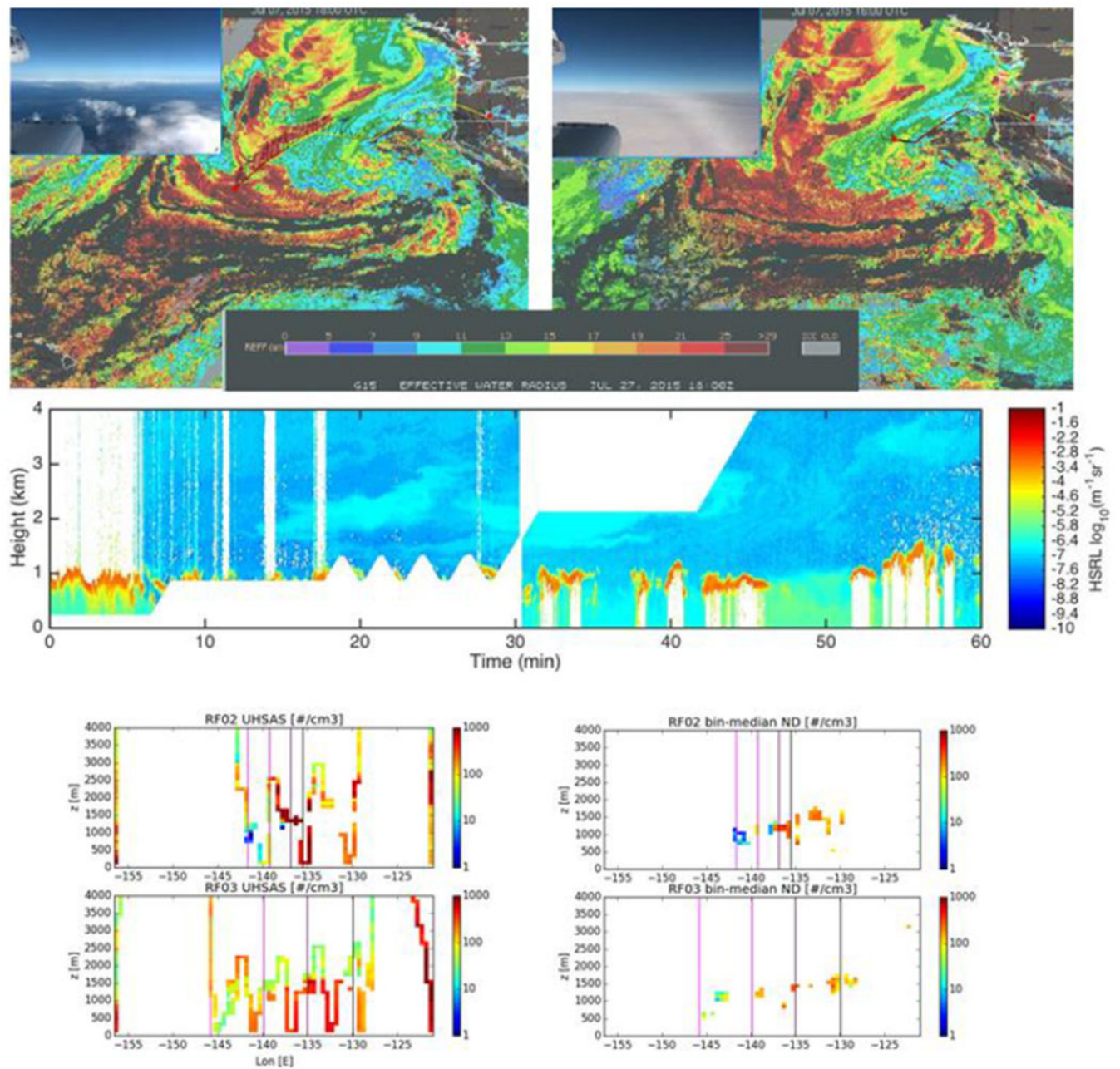


Figure 9:

Soundings from G-V ascents and descents comparing the thermodynamic and wind structure differences between equivalent air masses sampled on outbound RF-10 on segments BC in Fig. 7a and on inbound RF-11 BC segments shown in Fig. 7b.

**Figure 10:**

Effective droplet radius from GOES analyses for the outbound RF02 on July 7 at 1600 and 1800 UTC. The path of the G-V is indicated by a yellow line where the red marker at the end of the line is the location of the G-V. Photos from camera on G-V and the GOES images are from screenshots of the Field Catalog. The HSRL scattering returns are for the hour starting at 1700 UTC. The GV flight path is shown by yellow line and aircraft location by red dot. The UHAS particle concentrations and the median cloud droplet sizes from the cloud probe are shown as functions of longitude and altitude on both the RF02 outbound and RF03 inbound flights.

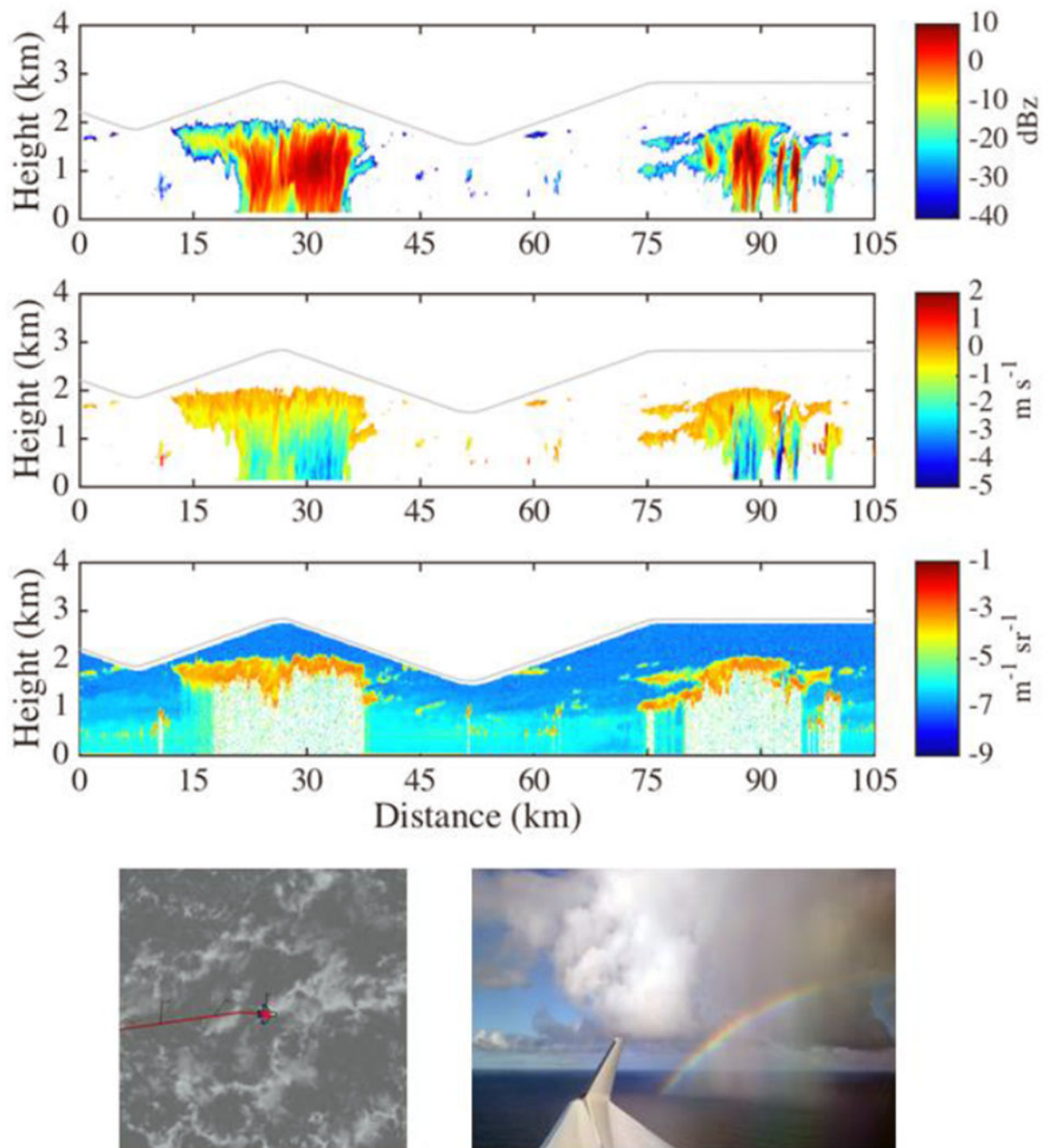


Figure 11:

HCR and HSRL returns from mesoscale cloud and precipitation complexes observed on RF-07 (July 19 2015) at 1910–1920 UTC. GOES high-definition visible image for this time period showing location of the aircraft near the time of the measurements. The photo of rainbow was taken on a 500' leg at 1802 UTC (courtesy of Jonathan Emmett).

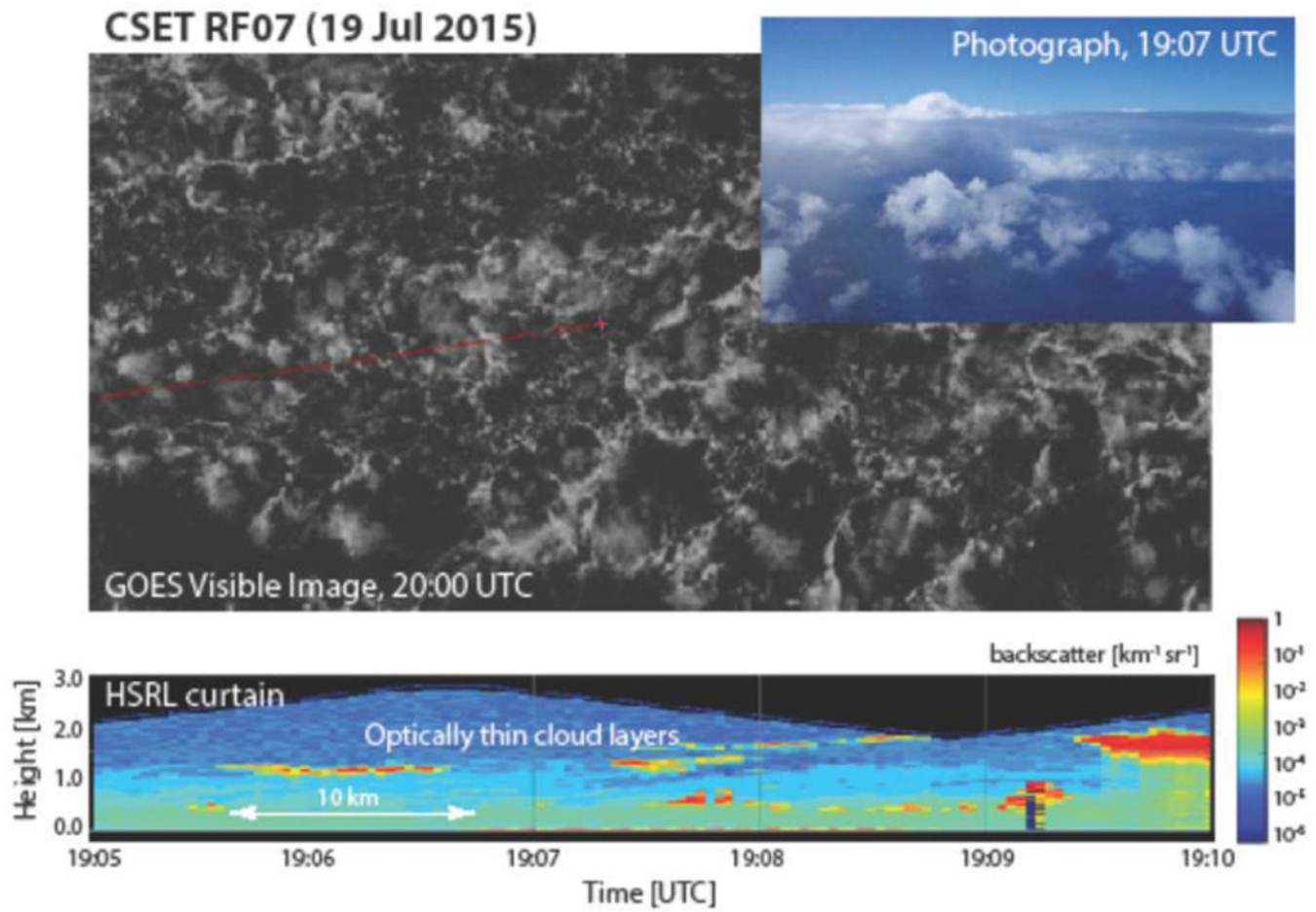


Figure 12:

Optically thin clouds and ultra clean layers sampled from GV on 19 July 2015 by HSRL starting at 1900 UTC. Path of aircraft during these measurements is overlaid (red line) on high resolution visible GOES image at same time. Photo was taken at 1905 UTC from GV.

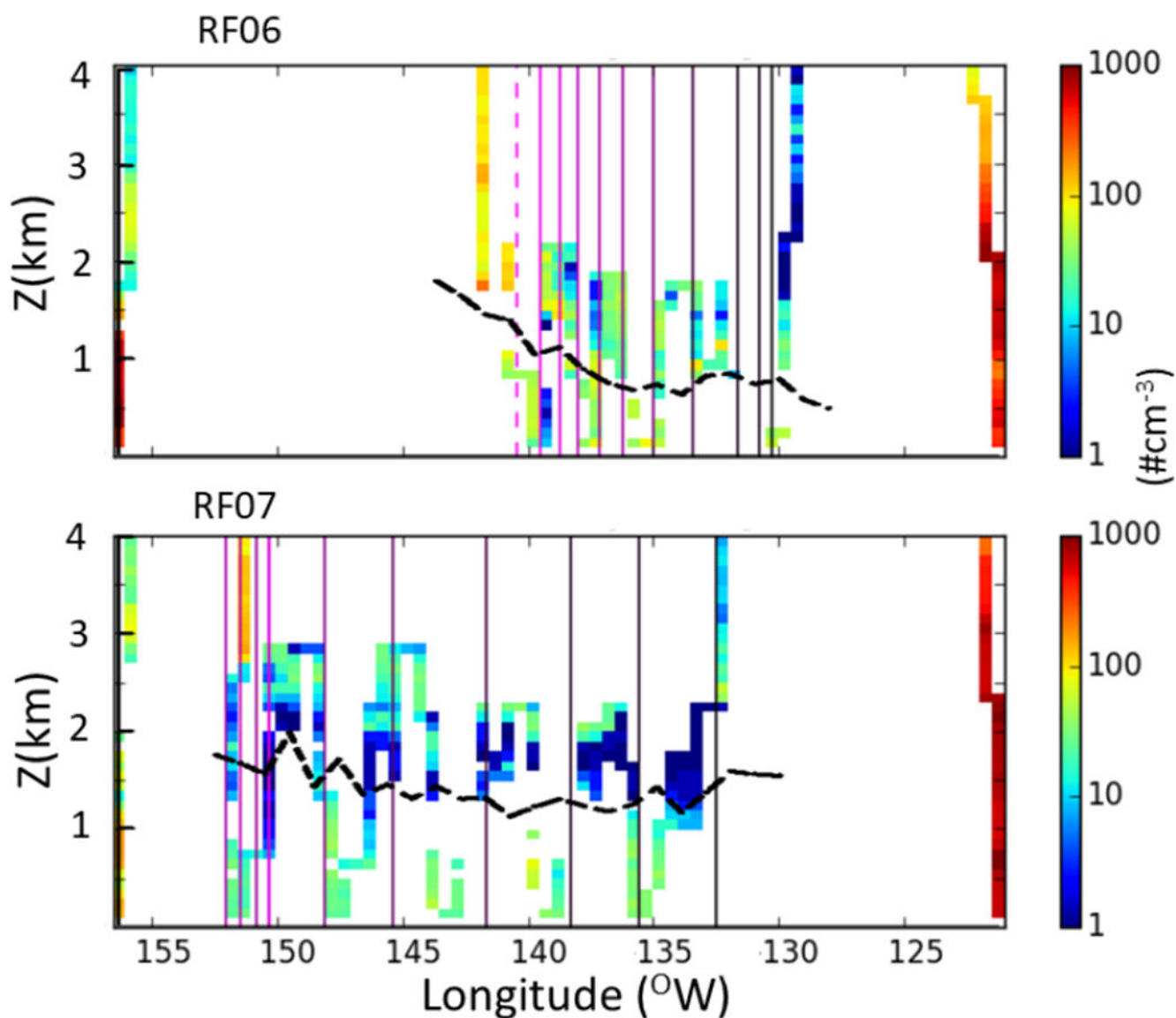


Figure 13: UHSAS aerosol concentrations observed on outbound July 7 (RF06) and inbound July 9 (RF07) flight showing dominance of ultra clean layer (UHSAS concentration of $<10 \text{ cm}^{-3}$) near cloud top on return flight RF07. The dashed black line is the cloud top height from (Schwartz, 2018). Some of the UHSAS points missing below the top are from samples made within the cloud where aerosol measurements tend to be unreliable.

Table 1:

GV Instrumentation for CSET

Instrument or Observing System	Parameters Measured and Range	
Thermometer (102AL TAT)	temp	
Dewpoint Hygrometer (BUCK 1011C)	dewpoint temperature	
Vertical Cavity Surface Emitting LASER Hygrometer (VCSEL)	water vapor concentration	
Winds (gust measurements; aircraft motion and position)	3-D wind components	
Cloud Droplet Probe (CDP)	cloud droplet spectra (2-50 μm)	
Three-view Cloud Particle Imager (3V-CPI)	cloud droplet spectra (15-250 μm)	
Two-Dimensional Optical Array Probe (2D-C)	cloud and drizzle droplet spectra (60-3200 μm)	
HOLODEC	cloud and drizzle ((6 μm – 1 mm)	
Ultra-High Sensitivity Aerosol Spectrometer (UHSAS)	aerosol spectra (60-1000 nm)	
Cloud Nuclei Counter (CN)	aerosol concentrations (>11 nm)	
King probe	cloud liquid water content	
Heinmann Infrared Radiation Pyrometer	sea surface temperature	
Microwave Temperature Profiler (MTP)	vertical temperature profile	
Broadband SW and LW Radiometers (Kipp & Zonnen)	upward and downward irradiances	
HIAPER Airborne Radiation (HARP)	downward spectral radiances	
Digital Cameras (on right and left Wing)	forward looking images	
Airborne Vertical Atmospheric Profiling System (AVAPS)	dropsonde signal processor	
HIAPER Cloud Radar (HCR; 95 GHz)	reflectivity, spectral width, Doppler velocity, raw I and Q	
G-Band Microwave Radiometer (183 GHz)	liquid water path	
High Spectral Resolution LIDAR (HSRL)	backscatter and linear depolarization	
Fast Response Ozone (FO3_AD)	Ozone mixing ratio	
Carbon Monoxide (Aereo-Laser VUV)	carbon monoxide	
Dropsondes	temp, humidity, and wind profiles	

Table 2:

Dates for research flight couplets with latitude and longitude positions of trajectory start areas (blue circles) and end areas (red circles) 2 days later plotted in Fig 5. Two sampling areas were identified on RF02-RF07. Three were identified on RF08-RF15.

Flight	West Bound: WB East Bound: (EB)	Dates	Lat 1 (°N)	Lon 1 (°E)	Lat 2 (°N)	Lon 2 (°E)	Lat 3 (°N)	Lon 3 (°E)
RF02	WB	7/7/2015	36.6	-136.7	34.0	-141.6		
RF03	EB	7/9/2015	28.6	-133.9	27.5	-142.6		
RF04	WB	7/12/2015	31.8	-130.6	28.4	-137.1		
RF05	EB	7/14/2015	27.9	-136.4	25.0	-146.4		
RF06	WB	7/17/2015	39.0	-131.5	34.49	-137.0		
RF07	EB	7/19/2015	27.2	-140.2	25.23	-149.5		
RF08	WB	7/22/2015	38.1	-128.4	35.9	-132.9	31.7	-138.4
RF09	EB	7/24/2015	28.3	-138.0	28.1	-147.4	25.1	-151.4
RF10	WB	7/27/2015	33.5	-129.6	29.7	-133.9	26.5	-140.0
RF11	EB	7/29/2015	28.5	-140.4	27.0	-146.8	23.7	-151.5
RF12	WB	8/01/2015	42.0	-130.0	40.8	-134.3	38.74	-138.1
RF13	EB	8/03/2015	33.5	-136.3	32.2	-142.6	30.02	-147.8
RF14	WB	8/07/2015	37.9	-131.9	34.7	-134.7	29.8	-137.8
RF15	EB	8/09/2015	28.5	-141.0	26.5	-148.3	23.4	-151.5